

**MAX-PLANCK-INSTITUT FÜR PLASMAPHYSIK**  
**GARCHING BEI MÜNCHEN**

**Neuere Entwicklungen in der  
niederenergetischen Inversen Photoemission**

Topics in Low-Energy  
Inverse Photoemission

**Ralf Schneider, Volker Dose**

IPP 9/79

Mai 1990

*Die nachstehende Arbeit wurde im Rahmen des Vertrages zwischen dem  
Max-Planck-Institut für Plasmaphysik und der Europäischen Atomgemeinschaft über die  
Zusammenarbeit auf dem Gebiete der Plasmaphysik durchgeführt.*

Mai 1990

**Abstract:**

Mehr als eine Dekade an Arbeit auf dem Gebiet der Inversen Photoemission (IPE) hat diesen Forschungsbereich wesentlich erweitert. Ursprünglich orientierte sich die Entwicklung an bekannten Resultaten der normalen Photoemission (PES), die einfach nur für den Fall unbesetzter Zustände reproduziert wurden. Nach und nach traten Probleme auf und wurden mit IPE angegangen, die keinen Vorläufer in normaler PES hatten. Die jetzige Situation ist durch eine vollständige Äquivalenz von PES und IPE charakterisiert. Konsequenterweise bestimmt die physikalische Fragestellung die Wahl der Technik. In diesem Sinne wollen wir neuere Entwicklungen in der Bandstrukturspektroskopie vorstellen, die in diesem Zusammenhang nur mit IPE Daten zu beantworten sind.

Wir diskutieren die Bestimmung von sowohl Volumen- als auch Oberflächen-Energiezuständen in Spiegelebenen. Die beobachteten Volumenübergänge werden mit theoretischen Vorhersagen einer Combined-Interpolation-Scheme Rechnung für die optischen Kurven in der projizierten Bandstruktur verglichen.

Für Messungen der Winkelverteilung der Strahlung in IPE muß man den Photonennachweiswinkel verändern können. Es wird gezeigt, daß die Winkelverteilung der Strahlung sehr gut dem Dipolmodell folgt, das eine quadratische Sinusabhängigkeit der Intensität des Übergangs vom Photonennachweiswinkel relativ zur Orientierung des Übergangsdipols vorhersagt. Zusätzlich werden die Meßdaten durch die Transmissionswahrscheinlichkeit der Photonen durch die Festkörper-Vakuum Grenzfläche modifiziert, die qualitativ den klassischen Fresnelformeln folgt.

Elektronische Zustände, die durch Adsorbate auftreten, werden als verallgemeinerte "Oberflächen"-Zustände diskutiert. Unsere Definition schließt auch Oberflächenumklappprozesse ein. Diese treten auf, da sich die Oberflächengeometrie und Symmetrie durch ein Adsorbat ändert, wodurch sich die Bedingungen für die dem Strahlungsübergang vorausgehende Beugung ändert. Volumenzustände können durch Oberflächenumklapps sichtbar werden. Wir zeigen, daß der Unterschied zwischen Volumen-, Oberflächen- und Adsorbatzuständen rein künstlich ist.

Es wird gezeigt, daß die Temperaturabhängigkeit der Intensität hauptsächlich durch Oberflächenschwingungen bestimmt wird. Dies wird bewiesen durch den Vergleich mittlerer quadratischer Auslenkungen, die aus der Temperaturabhängigkeit von IPE Volumenzuständen auf verschiedenen Oberflächen und aus Streuexperimenten, die auf Schwingungen in der Oberfläche empfindlich sind, bestimmt werden

Wir beschließen den Report mit einer Diskussion neuerer Resultate aus IPE Experimenten mit spinpolarisierten Elektronen, die auf ferromagnetische Proben auftreten.

¶ Dieser Report ist identisch zu einem Beitrag zu Topics in Applied Physics (Ed.: J. C. Fuggle) (Springer, Heidelberg, Berlin).

May 1990

**Abstract:**

More than a decade of work on inverse photoemission (IPE) has considerably advanced the field of research. Initially the development was oriented along known results from ordinary photoemission (PES), which were simply reproduced for the case of unoccupied levels. Gradually, problems arose and were tackled which had no predecessor in ordinary PES. The present situation is characterized by a full equivalency of PES and IPE. Consequently, the physical problem dominates over the choice of technique. In this sense we attempt to raise some recent topics in band structure spectroscopy, which, in the present context draw exclusively on IPE data.

We will discuss the band mapping in mirror planes for bulk and surface states. The observed bulk transitions will be compared with theoretical predictions for the optical curves in projected bulk band structure of a combined-interpolation-scheme calculation.

Measurements of the angular distribution of the radiation in IPE require the variation of photon take-off angle. As will be shown the radiation angular distribution follows quite well the dipole model, resulting in a squared sine function dependence of the intensity of the transition from the photon take-off angle relative to the orientation of the transition dipole. In addition the data are modified by the transmission probability of photons through the solid-vacuum interface, qualitatively following the classical Fresnel formulas.

Electronic states created by adsorbates are discussed as generalized "surface" states. Our definition includes surface umklapp processes. These occur because of the change of the surface geometry and symmetry by an adsorbate leading to different diffraction possibilities prior to the radiative transition. Bulk transitions can become visible through surface umklapps. We will show, that the difference of bulk, surface and adsorbate states is purely artificial.

The temperature dependence of intensities will be shown to be mainly due to surface vibrations. This is proved by comparing the mean square displacements extracted from the temperature dependence of IPE bulk transitions on different surfaces and from scattering experiments, which are sensitive to vibrations in the surface.

We conclude the report with a discussion of recent results from IPE experiments with spin polarized electrons impinging on ferromagnetic samples.

¶ This report is identical to a contribution to Topics in Applied Physics (Ed.: J. C. Fuggle) (Springer, Heidelberg, Berlin).

## Topics in Low-Energy Inverse Photoemission

1. Introduction	1
1.1. Basic concept of IPE	1
1.2. Intent of this paper	2
2. Band mapping in mirror planes	4
3. Radiation angular distribution	11
4. Adsorbate-induced states	16
4.1. Surface umklapp	17
4.2. Ni(111) p(2x2)S	19
5. Temperature dependence of IPE	21
6. Spin-resolved IPE	25
7. References	28
8. Figures	31



## Topics in Low-Energy Inverse Photoemission

### 1. Introduction

More than a decade of work on inverse photoemission (IPE) has considerably advanced the field of research. Several surveys to the respective level of maturity have appeared [1.1-4]. Initially the development was oriented along known results from ordinary photoemission (PES), which were simply reproduced for the case of unoccupied levels. Gradually, problems arose and were tackled which had no predecessor in ordinary PES [1.5]. The present situation is characterized by a full equivalency of PES and IPE. Consequently, the physical problem dominates over the choice of technique. In this sense we attempt to raise some recent topics in band structure spectroscopy, which, in the present context draw exclusively on IPE data.

#### 1.1. Basic concept of IPE

IPE uses the effect that electrons impinging on a solid surface may emit radiation. This phenomenon is known since ninety years as X-ray emission. Due to the energy dependent small elastic mean free path of 10 to 20 Å of low energy electrons with kinetic energies below 30 eV [1.6] IPE is very surface-sensitive.

In IPE electrons with well-defined kinetic energies  $E_{\text{Kin}}$  and well-defined angle of incidence  $\theta$  impinge on the sample and couple to bulk states of the solid, which are lying above the vacuum level  $E_{\text{Vac}}$  of the sample. From the initial state with energy  $E_i$  and wavevector  $\mathbf{k}_i$  the electrons can decay via radiative transitions to other lower lying unoccupied electronic final states with energy  $E_f$  and wavevector  $\mathbf{k}_f$ . In the IPE experiment the emitted photons with a quantum energy  $\hbar\omega$  are detected for a photon take-off angle  $\alpha$ . For this process the conservation of energy reads

$$E_i = E_f + \hbar\omega \quad (1.1).$$

Using the momentum conservation for the radiative transition we obtain

$$\mathbf{k}_i = \mathbf{k}_f + \mathbf{G} + \mathbf{q} \quad (1.2),$$

where  $\mathbf{G}$  is a reciprocal lattice vector. For photon energies below about 100 eV the wavevector of the photon  $\mathbf{q}$  remains small compared to the size of the Brillouin zone, e.g.  $\mathbf{G}$  and  $\mathbf{q}$  can be neglected in the momentum balance. Therefore, in a reduced zone scheme (left part of Fig. (1.1)), the radiative transition occurs vertically ( $\mathbf{k}_i = \mathbf{k}_f$ ) as a so-called direct transition. In an IPE experiment with fixed photon-energy  $\hbar\omega$  the intensity of the radiation (count rate of the emitted photons) is measured as a function of the final state energy  $E_f$  (right part of Fig. (1.1)) for an angle of incidence  $\theta$  of the electrons and a photon take-off angle  $\alpha$ . In such a spectrum a peak should appear at energies  $E_f$ , where a direct transition between two bands separated by  $\hbar\omega$  is possible. The width of the peaks is determined by the finite lifetimes of the final states. The measured spectrum has its onset at the Fermi level  $E_F$  and shows an energy-dependent, nearly structureless background, which stems mainly from radiative transitions after electron-hole pair production. Superimposed on this background Fig. (1.1) shows two direct transitions.

## 1.2. Intent of this paper

The main aim of this paper is to show that the complete system (bulk with surface and vacuum) must be regarded to fully understand the IPE measurements.

In section 2 we will discuss the band mapping in mirror planes for bulk and surface states. The existence of the surface results in the fact that only the wavevector parallel to the surface  $\mathbf{k}_{\parallel}$  is a good quantum number, whereas the wavevector perpendicular to the surface  $\mathbf{k}_{\perp}$  is changed for the incoming electrons. The observed bulk transitions will be compared with

theoretical predictions for the optical curves in projected bulk band structure of a combined-interpolation-scheme calculation. If an identical transition can be observed on different surfaces this transition can be triangulated and  $E(\mathbf{k})$  can be obtained.

Measurements of the angular distribution of the radiation in IPE require the variation of photon take-off angle  $\alpha$ . As will be shown in section 3 the radiation angular distribution follows quite well the dipole model, resulting in a squared sine function dependence of the intensity of the transition from the photon take-off angle relative to the orientation of the transition dipole. In addition the data are modified by the transmission probability of photons through the solid-vacuum interface, qualitatively following the classical Fresnel formulas.

Electronic states created by adsorbates are discussed in section 4 as generalized "surface" states. Our definition includes surface umklapp processes. These occur because of the change of the surface geometry and symmetry by an adsorbate leading to different diffraction possibilities prior to the radiative transition. Bulk transitions can become visible through surface umklapps. For the identification of this effect, measurements with variable photon-energy are necessary. The influence of the bulk on adsorbate states is discussed, too. It shows clearly that the difference of bulk, surface and adsorbate states is purely artificial.

Temperature dependent IPE transitions will be presented in section 5. The temperature dependence of intensities will be shown to be mainly due to surface vibrations. This is proved by comparing the mean square displacements extracted from the temperature dependence of IPE bulk transitions on different surfaces and from scattering experiments, which are sensitive to vibrations in the surface.

We conclude our chapter with a discussion of recent results from IPE experiments with spin polarized electrons impinging on ferromagnetic samples.

## 2. Band mapping in mirror planes

We recall from section 1 that IPE in the ultraviolet spectral range is suitable to determine the final state energies  $E_f$  as a function of the angle of incidence  $\theta$  of the electrons. The wavevectors  $\mathbf{k}_i$  and  $\mathbf{k}_f$  entering momentum conservation (1.2) refer to the bulk solid whereas the initial conditions of the experiment specify only the wavevector  $\mathbf{K}$  in vacuum. Upon penetration of the vacuum-solid boundary the incident electron experiences a force of unknown magnitude normal to the surface. Therefore, the component of the wavevector in the solid perpendicular to the surface  $\mathbf{k}_\perp$  is greater than  $\mathbf{K}_\perp$  in the vacuum

$$\mathbf{k}_\perp > \mathbf{K}_\perp \quad (2.1).$$

The forces parallel to the surface are periodic and lead to diffraction such that

$$\mathbf{k}_{i,\parallel} = \mathbf{K}_{i,\parallel} + \mathbf{G}_\parallel \quad (2.2),$$

where  $\mathbf{G}_\parallel$  is a surface reciprocal lattice vector. At sufficiently low quantum energy  $\hbar\omega$  and hence initial energy the requirement that  $|\mathbf{k}_{i,\parallel} - \mathbf{G}_\parallel| \leq |\mathbf{K}_i|$  leads to a preference for  $\mathbf{G}_\parallel = 0$ .  $\mathbf{K}_{i,\parallel}$  is given by

$$K_{i,\parallel} = (2m/\hbar^2 (E_f + \hbar\omega - \phi_P))^{1/2} \sin \theta \quad (2.3),$$

where  $E_f$  is the final state energy with respect to the sample Fermi level and  $\phi_P$  is the sample work function. Therefore, one can extract from the experimental data the final state energies  $E_f$  as a function of the wavevector parallel to the surface,  $E_f(k_\parallel)$ . Comparing the measured  $E_f(k_\parallel)$  data with predicted transitions from bandstructure calculations is a very important test for these calculations. Since the band structure of even simple crystals is quite complicated at general points in reciprocal space the experiments are usually done in mirror planes. Figure (2.1) shows the bulk Brillouin zone of an fcc lattice. The shaded planes are the  $\Gamma XUL$  and  $\Gamma XWK$  mirror planes of the crystal. In these mirror planes different bands

may become degenerate. This reduces the complexity of the observed spectra. Also only transitions from even initial states can occur, because the wavefunction of the incoming electron is a plane wave and has even parity. It can therefore couple only to those bulk electronic wavefunctions which have also even parity [2.1]. This leads again to a reduction of the number of possible transitions and a concomitant simplification of the observed spectra.

The volume Brillouin zone is projected onto the surface Brillouin zone as shown in Fig. (2.1) for a (100) surface of an fcc crystal. The two mirror planes  $\Gamma XUL$  and  $\Gamma XWK$  correspond to the  $\overline{\Gamma X}$  and  $\overline{\Gamma M}$  directions of the surface Brillouin zone in Fig. (2.1). Figure (2.2) shows experimental IPE spectra for Cu (100). The quantum energy is 9.6 eV [2.2]. Three sets of experimental spectra are shown for three photon take-off angles  $\alpha = 0^\circ, 35^\circ, 75^\circ$  and a variation of the polar angle of incidence  $\theta$  in the  $\overline{\Gamma X}$  direction. Measurements with constant photon take-off angle  $\alpha$  are possible by a rotatable electron-gun and a independently rotatable sample [2.3]. The intensity of the observed radiation is displayed as a function of final state energy  $E_f$ . Seven different emission features are present. The peaks B1-B4 are transitions into bulk states, whereas S1-S3 are transitions into surface states. This identification will be discussed later. The measurement at different photon take-off angle  $\alpha$  allows a separation of B2 and S3 [2.4], which have strongly different radiation angular distributions (see section 3). From the spectra of Fig. (2.2) one can extract the experimental  $E_f(k_{||})$  data. These are shown in Fig. (2.3) for energies up to 8 eV as filled and open symbols with error bars for transitions into bulk and surface states, respectively. Data for the  $\Gamma XWK$  mirror plane are also included. Open symbols without error bars are transitions predicted by a combined interpolation scheme calculation [2.3, 5]. The size of the symbols indicates the intensity of the transition.

We shall now attempt to interpret the measured bulk transitions in the frame of the well known three step model [2.6]. It has been developed for PES [2.7] and was then transferred to IPE [2.8]. This model divides the process into three steps:

1. The incoming electrons couple to a bulk band of the crystal
2. From the initial state  $E_i(\mathbf{k}_i)$  electrons are lost by non-radiative decay in the crystal
3. A direct optical transition occurs.

The intensity  $I$  for photons with energy  $\hbar\omega$  and for incoming electrons with energy  $E$  can be expressed as

$$I(\hbar\omega, E) \sim \sum_{i,f} \int_{\Omega} d^3\mathbf{k} |M_{fi}|^2 c_i \delta(E_i(\mathbf{k}) - E_f(\mathbf{k}) - \hbar\omega) \delta(E - E_i(\mathbf{k})) \quad (2.4).$$

The first  $\delta$ -function in (2.4) generates the conservation of energy (1.1). The second  $\delta$ -function defines the energy of the initial state as the energy of the incoming electron. The coupling probability to bulk bands is expressed by the coefficients  $c_i$ . These are expected to be large if a bulk band is free-electron-like [2.5]. The transition matrix-elements for PES and IPE  $M_{fi}$  are determined by the operator  $\mathbf{A}\mathbf{p}$  [2.9] (see section 3), the scalar product of the vector potential  $\mathbf{A}$  and the momentum operator  $\mathbf{p}$ . For radiation with wavelength  $\lambda$  such that  $\lambda/a \ll 1$  where  $a$  is the lattice constant of the crystal, the variation of the vector potential across the unit cell can be neglected and the dipole approximation is obtained [2.10]. Its practical validity extends to well beyond 100 eV. The transition matrix-element is then determined by the momentum matrix element  $\mathbf{p}_{fi}$ . Calculating  $\mathbf{p}_{fi}$  gives the intensity of the transition and the orientation of the transition dipole. All subsequent calculations of the momentum matrix elements  $\mathbf{p}_{fi}$  are based on the combined interpolation scheme [2.11], which was fitted at high symmetry points to a self-consistent bandstructure calculation of Bross et al. [2.12].

Figure (2.4) displays the  $\mathbf{k}$ -space location of the possible transitions with a



photon energy of 9.6 eV from even initial states into final states in the energy range -1 to 8 eV in the two mirror planes. The transitions from odd initial states have been omitted since they cannot be observed in the IPE experiments (see previous discussion). The arrows in Fig. (2.4) indicate the direction of the surface normals for the three low-index surfaces (100), (110) and (111). The different symbols belong to transitions between different bands, characterized by the respective dominant plane wave component of the wavefunction of the initial and final state. Most of the calculated transitions have too small matrix elements to be visible in the experiment. The main transition is the bulk transition marked with a diamond (B1) ( $\mathbf{G}_i = (0\ 0\ \bar{2})$ ,  $\mathbf{G}_f = (0\ 0\ 0)$ ). The second experimentally observed bulk transition B2 has  $\mathbf{G}_i = (\bar{1}\ \bar{1}\ 1)$  and  $\mathbf{G}_f = (\bar{1}\ \bar{1}\ \bar{1})$ . Within a simple two-band model [2.8] the momentum matrix element  $\mathbf{p}$  is determined by the exchanged reciprocal lattice vector  $\mathbf{G}$ , which is the difference between the initial state reciprocal lattice vector  $\mathbf{G}_i$  and the final state reciprocal lattice vector  $\mathbf{G}_f$

$$\mathbf{p} = \mathbf{G} V_{\mathbf{G}} / \omega. \quad (2.5)$$

$V_{\mathbf{G}}$  is the coefficient of the plane wave  $\exp(i\mathbf{G}\mathbf{r})$  in the Fourier expansion of the crystal potential.  $V_{\mathbf{G}} \exp(i\mathbf{G}\mathbf{r})$  mediates a transition between the two free-electron-like sp-bands. The size of the symbols in Figs. (2.3) and (2.4) is scaled with the square of the calculated dipole matrix element. Intensity changes of transitions characterized by identical exchanged reciprocal lattice vector indicate the inadequacy of the two-band model, where one would expect from (2.5) a constant intensity for these transitions.

The predicted dipole orientation for the transitions can be checked experimentally as will be discussed in the next section. Together with a very good overall agreement in the  $E(k_{\parallel})$ -curves for the bulk transitions a highly reliable determination of the reciprocal lattice vectors  $\mathbf{G}$ , exchanged in the transition, is obtained. The results of this analysis

provides the basis for the discussion of chapter 5.

The existence of the surface complicates the discussion. The coupling of the incoming electron to the initial state can change the observed intensity compared to the predicted intensity. This effect can be quite large, such that the order of intensities as obtained from the combined interpolation scheme calculation can even be reversed. An example for the importance of initial state coupling effects is contained in Fig. (2.3). Choosing a normalization such that observed and calculated intensities for bulk transition B1 match approximately we find a considerable discrepancy for B2. Obviously, the initial state coupling probability is much higher for B2 than for B1.

Band gaps of the projected bulk band structure are shown in Fig. (2.3) as grey shaded areas. The transitions into surface states are marked as open symbols with error bars. The surface states, lying in or close to the band gaps, can be divided into two classes [2.13]. For the barrier-induced surface states (S1) at normal incidence at 4.1 eV the probability density peaks in front of the surface in the vacuum. Barrier-induced surface states result from the long-range image-potential which an electron experiences in front of a surface. These (in brief) image states form Rydberg series of bound states close to the vacuum level. The crystal-induced surface states (S2, S3) are sensitive to the potential at the surface and their probability density peaks in the first surface layers. Both kinds of surface states have been discussed extensively in the literature [2.9, 10]. In Fig. (2.3) the continuous-line parabolas indicate the dispersion of the surface states. For these parabolas, if necessary, PES results have also been used [2.14].

If a particular transition can be seen on different surfaces the full  $E(\mathbf{k})$  dispersion can be compared between experiment and theory [2.15-17]. For copper we find at higher energy a bulk transition which can be seen on Cu(110) and (111). On Cu(111) it shows up only in the  $\overline{\Gamma M}$  ( $\Gamma KL$ ) direction due to the initial state effect discussed before, because the coupling of the



initial state wavefunction to the bulk states is different for  $\overline{\Gamma M}$  and  $\overline{\Gamma M'}$  ( $\Gamma XUL$ ). This results in  $\overline{\Gamma M'}$  direction in a total invisibility of this transition, although the matrix element is the same as in  $\overline{\Gamma M}$  direction. In Fig. (2.5) the  $E(k_{\parallel})$ -dispersion of this bulk state on Cu(110) (squares) and on Cu(111) in  $\overline{\Gamma M}$  direction (diamonds) is shown.

The triangulation is performed in the following way: From Fig. (2.5) one extracts pairs of  $k_{\parallel}$ -values for the (110) and (111) surface for a given final state energy (hence the alternative appellation 'energy coincidence method'). The respective  $k_{\parallel}$  defines a (dashed) line in Fig. (2.6) parallel to the (110) and (111) direction indicated by the light arrows. The fat arrows indicate the  $k_{\parallel}$ -directions for the (110) and (111) surface in the mirror plane. The filled diamonds at the intersections of these lines are the desired absolute k-space locations of the transitions. The size of the diamonds indicates the experimental error in the triangulation, resulting from the uncertainty in the energy and  $k_{\parallel}$ . The uncertainty in the energy is shown in Fig. (2.5), whereas the error in  $k_{\parallel}$  is  $0.1 \text{ \AA}^{-1}$  due to the limited angular resolution of the electron gun of  $\pm 2^{\circ}$ . The open symbols in Figs. (2.5) and (2.6) represent calculated results. From these calculations the initial and final state characters have also been identified to be predominantly  $(1 \ 1 \ \overline{1})$  and  $(\overline{1} \ 1 \ \overline{1})$  respectively. In contrast to the experimental observation two branches are predicted for the (111) surface. Failure to observe the predicted second branch is attributed to unfavourable initial state coupling. The experimental triangulation results show a good agreement with the combined-interpolation scheme calculation (open diamonds). This very same transition will be used in the section 5 to discuss the strong influence of surface effects on the temperature dependence of intensities of bulk transitions.

Finally, we want to note in this section that a nearly perfect description of the measured spectra [2.18] can be obtained in the one-step model [2.19] which

treats the measurement process of IPE (or PES) as one process in a multiple scattering formalism, including the scattering at the surface barrier.

### 3. Radiation angular distribution

An experimental validation of the dipole approximation is obtained by the measurement of the radiation angular distribution of a particular transition [3.1]. Such measurements also allow a polarization analysis which in turn provides a further stringent test on wavefunction symmetries. In the dipole approximation the transition matrix element  $M_{fi}$  is proportional to the product of the vectorpotential  $\mathbf{A}$  and the momentum matrix element  $\mathbf{p}_{fi}$

$$M_{fi} \sim \mathbf{A} \cdot \mathbf{p}_{fi} = A_x \langle \psi_f | \partial/\partial x | \psi_i \rangle + A_y \langle \psi_f | \partial/\partial y | \psi_i \rangle + A_z \langle \psi_f | \partial/\partial z | \psi_i \rangle \quad (3.1).$$

In Fig. (3.1) the expected angular dependence for pure  $A_x, A_y$  and  $A_z$  dipole transitions is shown. They should be described by a  $\sin^2 \delta$  law.  $\delta$  is the angle between the dipole axis and the direction of the photon emission.

Figure (3.2) shows a set of inverse photoemission spectra for various photon take-off angles  $\alpha$  normalized to equal intensity at a final state energy  $E_f$  of 5.7 eV. For the measurement of the angular distribution of the emitted radiation a rotatable electron gun was used. The electrons impinged at an angle  $\theta = -60^\circ$  relative to the surface normal of the Cu(100) crystal. Electrons as well as photons propagated in the  $\Gamma$ XUL mirror plane. We can identify two peaks in the spectra at 0.6 eV and 3.5 eV above the Fermi level. These transitions have been presented in section 2 as the two crystal-induced surface states (S2, S3) in the gap of the projected bulk band structure near the  $\bar{X}$  point of the surface Brillouin zone. The peaks remain stationary with changing photon take-off angle  $\alpha$  but show strong intensity variations. The higher energy peak vanishes completely for  $\alpha = -20^\circ$ . The top curve in Fig. (3.3) shows the intensity of the surface state at 3.5 eV as a function of the photon take-off angle  $\alpha$ . We see a broad maximum around  $\alpha = 30^\circ$ . The drop-off for large angles  $\alpha$  is similar to the behaviour of the background measured at 5.7 eV. We now assume that the angular dependence of the background represents the

transmission probability for the photons through the solid-vacuum interface. If we then normalize the intensity of the surface state emission to the background, we obtain the dotted curve in the bottom of Fig. (3.3) a. This curve should represent the emission probability for this transition as a function of photon take-off angle. A least squares fit to  $f(\delta) = A_x + A_{y,z} \sin^2 \delta$  reproduces the measured data excellently. In Fig. (3.3) b this data correction is shown as a polar plot. In this particular case we obtain further  $A_x=0$  as could be anticipated from Fig. (3.2) since the intensity of the transition disappear completely for  $\alpha = -20^\circ$ . The fit result  $A_x=0$  implies, that the transition dipole has no component perpendicular to the  $\Gamma$ XUL mirror plane. Symmetry selection rules for dipole transitions [3.2] in a mirror plane require that  $A_x$  or  $A_{y,z}$  is equal zero. The initial state wavefunction in the vacuum must always be even under reflection with respect to the mirror plane [3.3]. Since the matrix element must be invariant under the symmetry operation, even final states have a dipole axis lying in the mirror plane ( $A_x=0$ ;  $A_{y,z} \neq 0$ ). Odd final states have a dipole axis oriented normal to the mirror plane ( $A_x \neq 0$ ;  $A_{y,z}=0$ ). The data show conclusively, therefore, that this particular transition can be described as a dipole transition into an even final state and that there is no odd state at the same energy. The dipole axis encloses an angle of  $\sim 45^\circ$  with the surface normal. At the first glance this is somewhat surprising for a crystal induced surface state which owes its existence mainly to the potential step at the surface and should, therefore, have a dipole axis normal to the surface. However, away from normal incidence surface corrugation [3.4] introduces also x,y-components in the transition dipole, resulting in a dipole axis tilted away from the surface normal. For the particular case for the transition in Fig. (3.3) the dipole axis is oriented approximately parallel to the incident (or refracted) electron beam, reminiscent of the classical picture of bremsstrahlung emission by a

decelerated electron (see Fig. (3.3) b).

In Fig. (3.4) the experimental data on Cu(100) in the  $\Gamma$ XUL mirror plane for the dispersion of transitions with 9.6 eV photon energy (lower part) and the orientation of the dipole axis of these transitions (upper part) are compared with the results of the combined interpolation scheme. The shaded area indicates the projection of the bulk energy bands onto the Cu(100) surface. The combined interpolation scheme was used to calculate all bulk transitions at 9.6 eV photon energy with even initial state. These are shown by the dark bands in Fig. (3.4). The dispersion agrees well with the measured bulk states. The width of the bands corresponds to the calculated intensity of the transition. All observed transitions are into even final states which means all the dipole axes lie in the  $\Gamma$ XUL mirror plane. For the experimental data the dipole axis is determined by fits like the one shown in the bottom part of Fig. (3.3) a. These fits yield also the maximum intensity of the dipole emission, which is represented by the size of the symbols. The intensities agree qualitatively with the calculations. For the bulk transitions the measured orientation of the dipole axis follows approximately the calculated lines, but is shifted  $\sim 20^\circ$  away from the surface normal. This discrepancy for bulk states is not a shortcoming of the combined interpolation scheme but persists also with theoretical results from the IPE one-step model [3.5]. Such data are shown by filled symbols in Fig. (3.4). For the surface states (data points outside the shaded regions in the bottom part of Fig. (3.4)) only one calculated data point (S) is available showing also a  $\sim 20^\circ$  deviation from the experimentally determined dipole orientation. Since this discrepancy is observed for almost all data points, we have to discuss the possibility of a systematic error or omission in the data analysis. The quality of the fits allows the determination of the angle to  $5^\circ$  or better (see Fig. (3.3) a). The most critical assumption is the normalization of the data to the background as shown in Fig. (3.3) a. In order to access the background angular

distribution the simplest model for the transmission of light through an interface is the classical Fresnel formulae [3.6]. In Fig. (3.5) the calculated transmission for copper at 9.6 eV photon energy with the optical constants  $\epsilon_r = 0.35$  and  $\epsilon_i = 1.75$  [3.7] is shown for s ( $A_x = 0, A_{y,z} \neq 0$ ), p ( $A_x \neq 0, A_{y,z} = 0$ ) and unpolarised light. Assuming an unpolarised background we get the radiation characteristics of Fig. (3.6) (see Fig. (3.1) for comparison). The calculated transmission falls off more steeply at angles above  $60^\circ$  than the measured background curve. This holds also for optical constants far away from the above values. The above optical constants give total reflection for light impinging at an angle larger than  $37^\circ$  onto the solid-vacuum interface. We would observe, therefore, mainly transitions with a dipole axis oriented far away from the surface normal. This is in contrast to the observation which gives strong intensity for  $k_{\parallel} = 0$ . Symmetry considerations alone dictate a dipole axis parallel to the surface normal for  $k_{\parallel} = 0$ . If we include refraction as implied by Fresnel formulae in the data analysis procedure then we obtain considerably worse fits and an even larger discrepancy to the calculations. Fresnel corrections are obviously not suitable to describe our experimental results for inverse photoemission originating from the first few atomic layers of the surface. Local field theories of the electromagnetic field near a surface [3.8-9] give only small corrections to the Fresnel formulae which could not resolve the discrepancies.

For a possible explanation, we have to remember how the electromagnetic field is introduced into the Hamiltonian of the system. The momentum operator  $\mathbf{p}$  of the system without electromagnetic field is replaced by the generalised momentum  $\mathbf{p} - e/c \mathbf{A}$ . Neglecting the quadratic term in  $\mathbf{A}$  gives the transition matrix element  $M_{fi}$

$$M_{fi} = \langle \psi_f | \mathbf{A} \mathbf{p} + \mathbf{p} \mathbf{A} | \psi_i \rangle \quad (3.2),$$

where  $\psi_f$  and  $\psi_i$  are the exact many-body wavefunctions of the system.

Equation (3.2) can be rewritten to

$$M_{fi} = 2 \langle \psi_f | \mathbf{A} \mathbf{p} | \psi_i \rangle - i\hbar \langle \psi_f | \nabla \mathbf{A} | \psi_i \rangle \quad (3.3).$$

In practical calculations the exact wavefunctions are replaced by one-particle wavefunctions and the dipole approximation is used. In the normally used Coulomb calibration the second term of (3.3) is zero and the transition matrix element depends on  $\mathbf{A} \mathbf{p}$  as discussed before. Many-body effects can be included in the vector-potential  $\mathbf{A}$ , which is the dielectric response of the system to the radiation field [3.10]. But the second term is not equal to zero if longitudinal electromagnetic waves (plasmons in solids) or rapidly changing transversal fields (due to the surface barrier) exist. Therefore the second term can contribute to the transition matrix element and perhaps this gives the correction for the theoretical calculated data.



#### 4. Adsorbate-induced states

The study of the bonding of an adsorbate to a surface is motivated by the fact that nearly every chemical reaction with technical application takes place at the surface of catalysts. The first step of these reactions is the adsorption of the reaction partners. This very first step is a subject of considerable current research. IPE adds the possibility to study the adsorbate-induced unoccupied electronic states at surfaces. For a reduction of the complexity of the problem mostly well-ordered systems are studied. For the purpose of this chapter we define adsorbate-induced unoccupied electronic states as all states which emerge in the spectra after adsorption in addition to features of the clean surface. The adsorbate-induced states are a consequence of the additional three-dimensional potential of the adsorbate layer. In principle these states are equivalent to surface states which are produced by the approximately one-dimensional surface-barrier. Several 'types' of adsorbate-induced states can occur, although this classification is artificial because they are all produced by the total three-dimensional system adsorbate plus substrate.

1. The new geometry of the surface can produce surface umklapp processes. By the exchange of a reciprocal lattice vector of the adsorbate-covered surface, bulk states can appear in the spectra which are absent in the clean surface spectra.
2. The adsorbates intrinsic electronic states are influenced by direct adsorbate-adsorbate interaction at the surface or by indirect adsorbate-adsorbate interaction mediated by the substrate. This latter case has frequently been slighted by surface scientists. In case of substrate mediated adsorbate-adsorbate interaction electronic states may exhibit three-dimensional dispersion. The experimental results are then not only determined by the adsorbate layer symmetry but



also by the symmetry of the underlying substrate.

3. Due to the changed surface geometry the coupling of the incoming electron to the initial states changes. Normally this results in a strong intensity decrease of bulk direct transitions observed on the clean crystal. But sometimes bulk transitions with high transition matrix elements become visible upon formation of the adsorbate layer. Such states have escaped detection on the clean surface by the low coupling probability. This coupling probability is increased by the adsorbate.
4. The adsorbate-substrate system has a new surface potential compared to the clean surface. Therefore, surface states can shift, disappear or appear (a very recent example constitutes the hydrogen adsorption on Ni(110) [4.1]).

The remainder of this section will deal with examples to points one and two given above.

#### 4.1. Surface umklapp

As a first example illustrating the three-dimensionality of the problem we consider bulk direct transitions on Ni(110) both on the clean and adsorbate covered surface. A flexible apparatus is required allowing measurements at arbitrary k-points of the bulk Brillouin zone. In particular k-points differing only by the exchange of a surface reciprocal lattice vector must be accessible. In IPE (as in photoelectron spectroscopy) this requires variable quantum energy by using a monochromator [4.2-3]. In Fig. (4.1) IPE spectra of a Ni(110) surface with a sulphur (c(2x2)-S), chlorine (c(2x2)-Cl) and oxygen ((2x1)-O) adsorbate structure are shown. The spectra are measured with a monochromator with variable quantum energy for constant initial state energies from 16.8 eV up to 23.8 eV [4.4]. The spectra of the clean surface are shown as full lines for comparison. In the spectra of the clean surface with 23.8 eV initial state energy a direct bulk

transition can be seen as a weak structure at 2.9 eV above the Fermi energy [4.5]. The adsorption of sulphur, chlorine and oxygen suppresses this bulk transition. In the Ni(110) - c(2x2)S spectra another peak at 4.8 eV shows no variation of its peak position with the energy of the initial state. It is an adsorbate state of sulphur and will not be discussed here. We will focus on the additional emission at about 2 eV final state energy. This feature shows dispersion with the initial state energy  $E_i$  and therefore because of normal incidence condition with the wavevector perpendicular to the surface. This is a typical behaviour of a bulk electronic state. However, for normal incidence at  $\bar{\Gamma}$  ( $\Gamma$  ( $\Sigma$ ) K - line of the bulk) no bulk transitions in this final state energy range exist. Analogous spectra for the c(2x2)Cl and the c(2x2)S structure are identical for final state energies up to 3.5 eV to those observed on c(2x2)S. For the (2x1)O structure the additional emission at about 2 eV does not show up. We conclude that this emission is only determined by the periodicity of the surface. Due to the c(2x2) structure a surface umklapp can occur from  $\bar{\Gamma}$  to  $\bar{S}$  (L (Q) W - line of the volume). This again a  $\bar{\Gamma}$ -point of the SBZ of the adsorbate covered surface, hence equivalent to normal incidence for the adsorbate. The observed feature could therefore originate from  $\bar{\Gamma}$  or  $\bar{S}$  or both. For the substrate, however,  $\bar{S}$  is only accessible for normally incident electrons via diffraction exchanging a surface reciprocal lattice vector  $\mathbf{G}$ . A series of spectra of the clean surface for the  $\bar{S}$ -point measured by suitable choice of the angle of incidence of the electrons for each initial state energy is shown in the lower right panel of Fig. (4.1). The arrows mark the transitions which are expected from combined interpolation scheme calculations. They agree well with observations. However, more important is the fact, that the spectra at the  $\bar{S}$ -point of the clean surface are identical to the spectra of the c(2x2)S and c(2x2)Cl structure. From this the adsorbate-induced emission can be identified as a surface umklapp process into a bulk band, unaccessible on the clean surface [4.4].

## 4.2. Ni(111) p(2x2)S

The adsorbate-induced states are not only determined by the symmetry of the adsorbate structure, but also by the bulk symmetry due to the interaction of the adsorbate with the substrate [4.6]. In Fig. (4.2) IPE spectra for the Ni(111) p(2x2)S structure measured with fixed photon energy of 9.6 eV are shown [4.6]. The transition close to the Fermi level is a transition into a d-band of nickel [4.7]. The structure at 1.7 eV at normal incidence is an adsorbate-induced state. This state disperses differently in  $\overline{\Gamma M}$  and  $\overline{\Gamma M'}$  direction. This could be explained by two transitions at different energies, which have different radiation characteristics (different dipole orientations). In order to rule out this possibility, spectra for an angle of incidence of the electrons of  $\theta = -20^\circ$  in  $\overline{\Gamma M}$  and  $\overline{\Gamma M'}$  direction were taken for the identical photon take-off angle  $\alpha = 25^\circ$ . In the experimental setup for these measurements it was not possible to rotate the electron gun. Fortunately, the sample could be rotated azimuthally about  $180^\circ$  from the  $\overline{\Gamma M}$  to the  $\overline{\Gamma M'}$  direction enabling measurements for identical  $\alpha$ . The spectra clearly show (Fig. (4.2)) that the asymmetric dispersion of the adsorbate-induced state is coupled to the coordinate system of the crystal and is not the result of different dipole orientations. The adsorbate layer has sixfold symmetry, whereas the [111] axis of the crystal has only threefold symmetry (Fig. (4.3)). The asymmetric dispersion cannot be explained by the potential of the two-dimensional adsorbate layer (direct adsorbate-adsorbate interaction). The time-reversal symmetry gives symmetric dispersion for a two-dimensional system, although the potential may be asymmetric, because a mirror plane is missing due to the threefold coordinated adsorption place of the sulphur. The conclusion is, that the asymmetric dispersion of the adsorbate-induced

state can only be explained by an interaction of the adsorbate with the bulk. This shows clearly the fact that adsorption problems are normally three-dimensional. Proper understanding of adsorbate induced states requires also a thorough consideration of substrate bulk states since IPE probes electronic states of the total system.

## 5. Temperature dependence of IPE

Especially in spin-polarised IPE temperature dependent studies are important for the study of magnetic phase transitions [5.1-3]. An understanding of the non-magnetic temperature effects is necessary for a discussion of the magnetic effects. In this section we will discuss the temperature dependence of IPE from the copper surfaces Cu(100), (110) and (111). An extensive discussion of the temperature dependence of IPE is given in [5.4]. We will focus here on the importance of the surface .

In Fig. (5.1) a typical set of temperature dependent IPE measurements is shown. For the temperature dependent measurements the photon take off angle  $\alpha$  was optimized to obtain maximum count rates. The main temperature effect is the reduction of the intensities of the transitions with increasing temperature. The background, indicated by the dashed line in Fig. (5.1), is found to be independent of temperature within the statistical error limits. The peak width and shape also do not show a temperature dependence, although the experimental setup was not able to detect small changes because of its limited resolution (full width at half maximum of the apparatus function is 0.7 eV [5.5]).

In Fig. (5.2) the temperature dependence of the direct transition into a bulk state, which has been triangulated from Cu(111) and (110) in section 2, is shown. We would expect the same temperature dependence for both surfaces if bulk effects are dominating the temperature dependence, because it is the identical bulk transition observed on different surfaces. The intensity on Cu(110) decreases much stronger than on Cu(111). In Fig. (5.3) the peak intensities of the triangulated transition and a bulk transition on Cu(100) were measured as a function of temperature during cooling down after heating the sample to 900 K. Several independent runs were accumulated to reduce the statistical error. The intensities were

corrected for the background, which was found to be independent of temperature within the statistical error limits. Possible bulk impurity segregation and contamination during experiment could be excluded by the comparison of IPE spectra before and after the temperature dependent measurements. The data points are plotted semilogarithmically versus temperature and can be fitted well by straight lines for the whole temperature range for Cu(111) and (100) and for temperatures below about 400 K for Cu(110). The statistical uncertainty is indicated by error bars, which are in most cases smaller than the size of the symbols. The normalization of the data points comes from the extrapolation of the straight line fits to  $T = 0$  K. The interpretation of the results can be attempted within a simple Debye-Waller Ansatz [5.6]

$$I = I_0 \exp(-\langle u^2 \rangle \Delta k^2), \quad (5.1)$$

where  $\langle u^2 \rangle$  is the mean square displacement of the atoms and  $\Delta k$  is the momentum exchanged in the transition. The mean square displacement can be expressed in the Debye-model [5.7] as

$$\langle u^2 \rangle = 3 \hbar^2 T / (M k_B \Theta_D^2). \quad (5.2)$$

Here,  $M$  is the mass of the atom,  $\Theta_D$  is the Debye temperature and  $k_B$  is Boltzmann's constant. The combination of Eqs. (5.1) and (5.2) gives immediately the exponential decrease of the intensity with temperature as shown by the straight line fits in Fig. (5.3). The momentum  $\Delta k$  is obtained from the calculations with the combined interpolation scheme of section 2 and by comparison of the experimental data with the calculated bulk transitions. Using Eq. (5.1) one can calculate the temperature dependence of the mean square displacements on the three copper surfaces from the IPE data of Figs. (5.2) and (5.3). The data for Cu(111) follow a linear dependence up to 800 K whereas the data for Cu(110) deviate from that linear dependence above 400 K. Inspection of Fig. (5.4) shows a surprisingly good agreement between IPE and results from helium atom

[5.8-9] and ion scattering [5.10]. The helium atom scattering data are corrected for correlated vibrations following [5.8]. For Cu(100) a deviation from the linear behaviour above 800 K can be found. Unfortunately one is not able to obtain IPE data in this temperature range because of evaporation of copper onto the entrance window of the detector. The IPE data on Cu(111) and (110) are multiplied by a factor of 0.35 and on Cu(001), which is a different transition, by a factor of 0.75 in order to correct for multiple scattering effects. The multiple scattering effects in IPE are similar to those known from LEED. They are not included in the simple model of Eq. (5.1). Multiple scattering enhance the mean square displacements as extracted from the IPE data, because if the incoming electron is multiply scattered it 'sums up' the vibration of many atoms and not only that of a single atom. The IPE data on Cu(111), where the scaling factor for this transition was determined by comparison with the results of the scattering experiments on Cu(110), agree also quite well with the mean square displacements of surface atoms, which are results of phonon slab calculations shown as full lines in Fig. (5.4) [5.11]. The deviation from the linear dependence may be due to the anharmonicity of the potential at the surface. This results in increased mean square displacements at the surfaces of Cu(001) and (110) above 800 K and 400 K, respectively.

Since the scattering experiments probe only the top surface layer the good agreement shows conclusively that the temperature dependence of IPE is influenced strongly by vibrations of the atoms in the surface layer. We would like to note here that the mean free path of electrons in our energy range is of about 10 Å corresponding to up to 5 layers. Surface specific effects should be dominating only in the first two or three layers with deeper layers showing essentially bulk behaviour.

The temperature dependence of IPE can be interpreted in the following picture: In an observed direct transition in IPE the incoming electron couples



to the initial bulk state and decays to the final state by producing a photon with the photon-energy of the detector. The temperature introduces vibrations of the lattice atoms. Therefore, the increasing scattering of electrons out of the initial state by the vibrating atoms with increasing temperature is the dominant temperature dependent process and results in a decrease of the intensity of the transition. This scattering is a multiple scattering process. The scattered electrons can decay to lower energies via radiative transitions with different photon energies or via Fermi surface excitations. Fermi surface excitations preceeding radiative transitions are believed to be responsible for the background in IPE spectra. The decreasing intensity of the direct transition need not result in an observable increase in the background, because in the decay of the scattered electron via a direct transition of different photon energy the electron is not detected and in the decay via processes producing the background of the IPE spectra the gain of intensity for the background is distributed over the whole solid angle of  $4\pi$ . The temperature dependence of IPE is determined by the vibrations of the surface atoms.



## 6. Spin-resolved IPE

For ferromagnetic materials like iron or nickel the spin degeneracy is removed from the electronic states and each band of the hypothetically nonmagnetic material appears as a twin in the magnetic state. A comprehensive description of electronic states in ferromagnetic crystalline solids requires therefore spin-resolution of energy versus momentum band dispersions. Spin-resolved IPE requires a spin-polarised electron beam, which can be produced by photoemission from GaAs [6.1]. In this section we will present spin-resolved IPE data on Ni(110) for an sp-bulk transition and for a transition into a crystal-induced surface state. Experimental details and a more extensive discussion is given in [6.2].

The magnetic moment per atom in bulk nickel is approximately  $0.55 \mu_B$ , where  $\mu_B$  is Bohr's magneton. The noninteger value of the magnetic moment proves that Ni is a bandferromagnet. At zero temperature the majority 3d-band states are fully occupied while the associated minority states with average occupation number 4.45 extend to energies slightly above the Fermi energy. Theoretical calculations predict a spin splitting of bulk transitions not only for d- but also for sp-like final bands due to hybridization [6.3]. In the case of a flat final band the measured spin splitting reflects directly the exchange splitting of the band. For steep final bands the measured spin splitting depends not only on the exchange splitting of the final band and its slope, but also on a possible though generally much smaller splitting of the initial state [6.4]. Furthermore, off normal incidence spin split features belong to slightly different values of  $k_{||}$  due to the different final state energies. As an example for the spin splitting of an sp-band Fig. (6.1) shows a bulk transition B on Ni(110) for an angle of incidence  $\theta$  of  $65^\circ$  [6.4]. The spin resolved data of Fig. (6.1) refer to a hypothetical polarization of the incident electron beam of 100%.

Let  $n_{\uparrow,\downarrow}$  represent the count rates for a beam with polarization  $P$ , and  $N_{\uparrow,\downarrow}$  the count rates expected for a hypothetical 100% polarized beam. The asymmetry  $A$  is then defined as

$$A = (N_{\uparrow} - N_{\downarrow}) / (N_{\uparrow} + N_{\downarrow}) = (n_{\uparrow} - n_{\downarrow}) / ((n_{\uparrow} + n_{\downarrow}) P \cos\phi) \quad (6.1).$$

using  $N = N_{\uparrow} + N_{\downarrow} = n_{\uparrow} + n_{\downarrow}$  we obtain

$$N_{\uparrow,\downarrow} = 0.5 N (1 \pm A) \quad (6.2).$$

$\phi$  in the above formula is the angle between the domain magnetization and the spin polarization vector. We want to emphasize here that the magnetization structure of the surface must be properly accounted for in all spin resolved electron spectroscopies. This point has not received proper attention in the past. The magnetic domain orientation on Ni(110) was verified by ex-situ magneto-optic Kerr measurements to point into the  $\langle 111 \rangle$  direction [6.4]. Let  $\gamma$  be the angle between  $\langle 111 \rangle$  and  $\langle 110 \rangle$  direction,  $\gamma \approx 35^\circ$ , then by using the addition theorem for spherical harmonics  $\cos\phi$  may be expressed as

$$\cos\phi = \cos\gamma \cos\theta \quad (6.3),$$

where  $\theta$  is the angle of incidence for the electrons. The spin polarization of the GaAs photoemitter used for the IPE measurements as spin-polarised electron source was  $P = 33\% = 0.27/\cos\gamma$ . From theory one would expect for the observed bulk transition at this value of  $k_{\parallel}$  a spectral splitting of 250 meV. The measurement is, however, carried out at constant  $\theta$ , not at constant  $k_{\parallel}$ . This reduce the expected splitting to about 150 meV in reasonable agreement with the observed  $(140 \pm 20)$  meV. Closer inspection of Fig. (6.1) shows that the line width of the spin "down" ( $\downarrow$  denotes majority) line is slightly larger than the spin "up" ( $\uparrow$  denotes minority). The shorter lifetime of the spin down state follows from the high density of empty spin down states near to the Fermi energy [6.5].

In Fig. (6.1) also the asymmetry  $A$  is shown as a function of the final state energy. It is important to note  $A$  changes sign in region of the direct

transition. This rules out an apparent spin splitting simulated by an unpolarized line superimposed on a polarized background.

Finally, we will discuss spin-resolved IPE data for a transition into a crystal induced surface state on Ni(110). As discussed before crystal induced surface states arise from a modification of the bulk electronic structure near the surface. Consequently they depend on the band structure of the material in question and are expected to show spin-splitting [6.6]. The probability density of crystal induced surface states peaks usually in the first atomic layer. The state  $S_1$  in Fig. (6.2) has been identified as such a crystal induced surface state. Figure (6.2) shows spectra of  $S_1$ , both spin-averaged and spin-resolved near  $\bar{X}$ . The spin-resolved data show a definite splitting. Since the energy of  $S_1$  is nearly independent of  $k_{\parallel}$  at  $\bar{X}$ , the observed splitting of  $(170 \pm 30)$  meV is equal to the final state exchange splitting. This is a considerable magnetic effect for a state 6 eV above the Fermi energy. Moreover, since  $S_1$  is localised in the first atomic layer its observed spin-splitting refutes magnetically dead surface layers on Ni(110) [6.4].

### Acknowledgements

The authors want to thank K. Desinger, M. Donath, H. Dürr and Th. Fauster for their contributions to this paper. Continuous financial support by the Deutsche Forschungsgemeinschaft is gratefully acknowledged.

## 7. References

- 1.1 P. T. Andrews, J. E. Inglesfield: to be published in the same volume as this article in Topics in Applied Physics (Springer, Berlin, Heidelberg).
- 1.2 V. Dose: Surf. Sci. Rep. 5, 337 (1985).
- 1.3 F. J. Himpsel: Comm. Cond. Mat. Phys. 12, 199 (1986).
- 1.4 N. V. Smith: Rep. Prog. Phys. 51, 1227 (1988).
- 1.5 V. Dose: J. Vac. Sci. Technol. A5, 2032 (1987).
- 1.6 M. P. Seah, and W. A. Dench: Surf. and Interface Analysis 1, 2 (1979).
- 2.1 J. Hermanson: Solid State Commun. 22, 9 (1977).
- 2.2 V. Dose, Th. Fauster, R. Schneider: Appl. Phys. A40, 203 (1986).
- 2.3 Th. Fauster, R. Schneider, and H. Dürr: Phys. Rev. B40, 7981 (1989).
- 2.4 M. Donath, M. Glöbl, B. Senftinger and V. Dose: Solid State Commun. 60, 237 (1986).
- 2.5 N. V. Smith: Phys. Rev. B19, 5019 (1979).
- 2.6 V. Dose: Prog. Surf. Sci. 13, 225 (1983).
- 2.7 C. N. Berglund, W. E. Spicer: Phys. Rev. 136, A1030 (1964).
- 2.8 D. P. Woodruff, N. V. Smith, P. D. Johnson, W. A. Royer: Phys. Rev. B26, 2943 (1982).
- 2.9 N. V. Smith: Rep. Prog. Phys. 51, 1227 (1988).
- 2.10 V. Dose: Surf. Sci. Rep. 5, 337 (1985).
- 2.11 N. V. Smith and L. F. Matheis: Phys. Rev. B9, 1341 (1974).
- 2.12 H. Bross and B. Schiek: private communication.
- 2.13 P. M. Echenique, J. B. Pendry: J. Phys. C11, 2065 (1978).
- 2.14 R. Schneider, H. Dürr, Th. Fauster, and V. Dose: for publication submitted to Phys. Rev. B.
- 2.15 E. O. Kane: Phys. Rev. Lett. 12, 97 (1964).

- 2.16 R. R. Turtle, T. A. Callcott: Phys. Rev. Lett. 34, 86 (1975).
- 2.17 A. Goldmann, M. Donath, W. Altmann, V. Dose: Phys. Rev. B32, 837 (1985).
- 2.18 J. B. Pendry: J. Phys. C14, 1381 (1981).
- 2.19 G. Borstel and G. Thörner: Surf. Sci. Rep. 8, 1 (1987).
- 3.1 Th. Fauster, R. Schneider, and H. Dürr: Phys. Rev. B40, 7981 (1989).
- 3.2 W. Eberhardt and F. J. Himpsel: Phys. Rev. B21, 5572 (1980) and Phys. Rev. B23, 5650 (1981).
- 3.3 J. Hermanson: Solid State Commun. 22, 9 (1977).
- 3.4 N. V. Smith: Phys. Rev. B14, 3549 (1985).
- 3.5 G. Borstel and G. Thörner: Surf. Sci. Rep. 8, 1 (1987).
- 3.6 J. D. Jackson: Classical Electrodynamics (Wiley, New York 1975).
- 3.7 J. H. Weaver, C. Krafka, D. W. Lynch, and E. E. Koch: DESY Report 41, HASYLAB 81/05 (1981).
- 3.8 F. Forstmann and R. R. Gerhardts: "Metal Optics Near the Plasma Frequency", in Springer Tracts Mod. Phys., Vol. 109 (Springer, Berlin, Heidelberg 1986).
- 3.9 P. J. Feibelman: Prog. Surf. Sci. 12, 287 (1987).
- 3.10 N. Barberan and J. E. Inglesfield: J. Phys. C14, 3114 (1981).
- 4.1 G. Rangelov, N. Memmel, E. Bertel, and V. Dose: for publication submitted to Surf. Sci..
- 4.2 Th. Fauster, D. Straub, J. J. Donelon, D. Grimm, A. Marx, and F. J. Himpsel: Rev. Sci. Instrum. 56, 1212 (1985).
- 4.3 V. Dose: "Instrumentation in Inverse Photoemission", in Lectures on Surface Science, ed. by G. R. Castro and M. Cardona (Springer, Berlin, Heidelberg 1987).
- 4.4 K. Desinger, W. Altmann, and V. Dose: Surf. Sci. 201, L491 (1988).
- 4.5 W. Altmann, K. Desinger, V. Dose, A. Goldmann: Solid State Commun. 65, 1411 (1988).

- 4.6 K. Desinger: IPP-Report 9/72, (1989).
- 4.7 A. Goldmann, M. Donath, W. Altmann, V. Dose: Phys. Rev. B32, 837 (1985).
- 5.1 M. Donath: Appl. Phys. A49, 351 (1989).
- 5.2 M. Donath and V. Dose: Europhys. Lett. 9, 821 (1989).
- 5.3 W. Nolting, W. Borgiel, V. Dose, and Th. Fauster: Phys. Rev. B40, 5015 (1989).
- 5.4 R. Schneider, H. Dürr, Th. Fauster, and V. Dose: for publication submitted to Phys. Rev. B.
- 5.5 V. Dose, Th. Fauster, R. Schneider: Appl. Phys. A40, 203 (1986).
- 5.6 N. J. Shevchik: Phys. Rev. B16, 3428 (1977), J. Phys. C, L555 (1977), Phys. Rev. B20, 3020 (1979).
- 5.7 N. W. Ashcroft, N. D. Mermin: Solid State Physics (Holt Saunders, London 1976).
- 5.8 D. Gorse and J. Lapujoulade: Surf. Sci. 162, 847 (1985).
- 5.9 P. Zeppenfeld, K. Kern, R. David, and G. Comsa: Phys. Rev. Lett. 62, 63 (1989).
- 5.10 H. Dürr, R. Schneider, Th. Fauster: in course of publication in Vacuum.
- 5.11 R. Schneider: IPP-Report 9/75, (1989).
- 6.1 U. Kolac, M. Donath, K. Ertl, H. Liebl, V. Dose: Rev. Sci. Instrum. 59, 1933 (1988).
- 6.2 M. Donath: Appl. Phys. A49, 351 (1989).
- 6.3 J. Noffke: private communication.
- 6.4 M. Donath, V. Dose, K. Ertl, and U. Kolac: in course of publication in Phys. Rev. B41, (1990).
- 6.5 R. Feder, A. Rodriguez: Solid State Commun. 50, 1033 (1984).
- 6.6 G. Borstel and G. Thörner: Surf. Sci. Rep. 8, 1 (1987).

## 8. Figures:

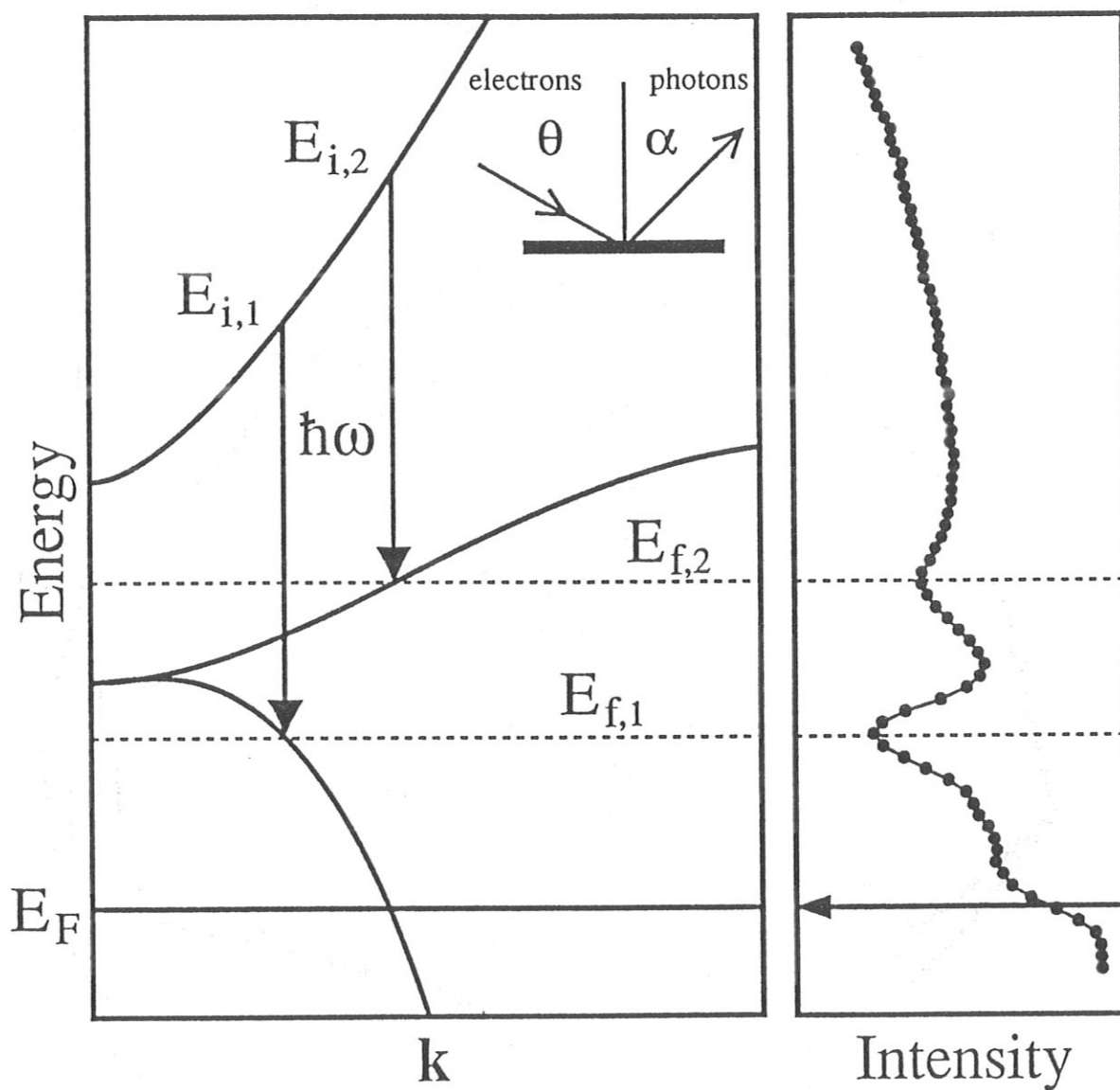


Figure (1.1):

Principle of inverse photoemission. A peak appears in the measured spectra, when the energy difference between initial and final state is equal to the quantum energy.

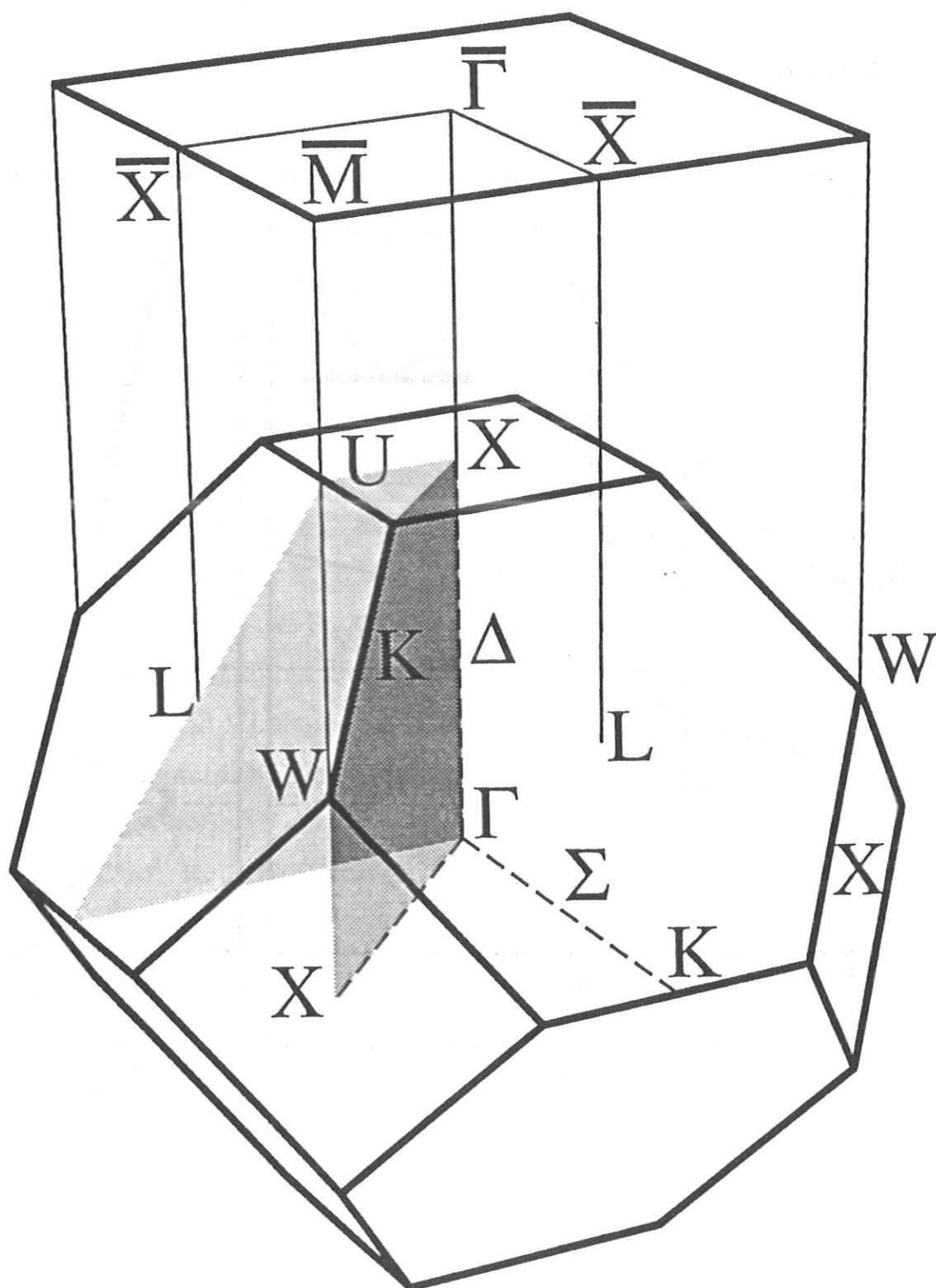


Figure (2.1):

Volume and surface brillouin zone of a face centered cubic (100) crystal.



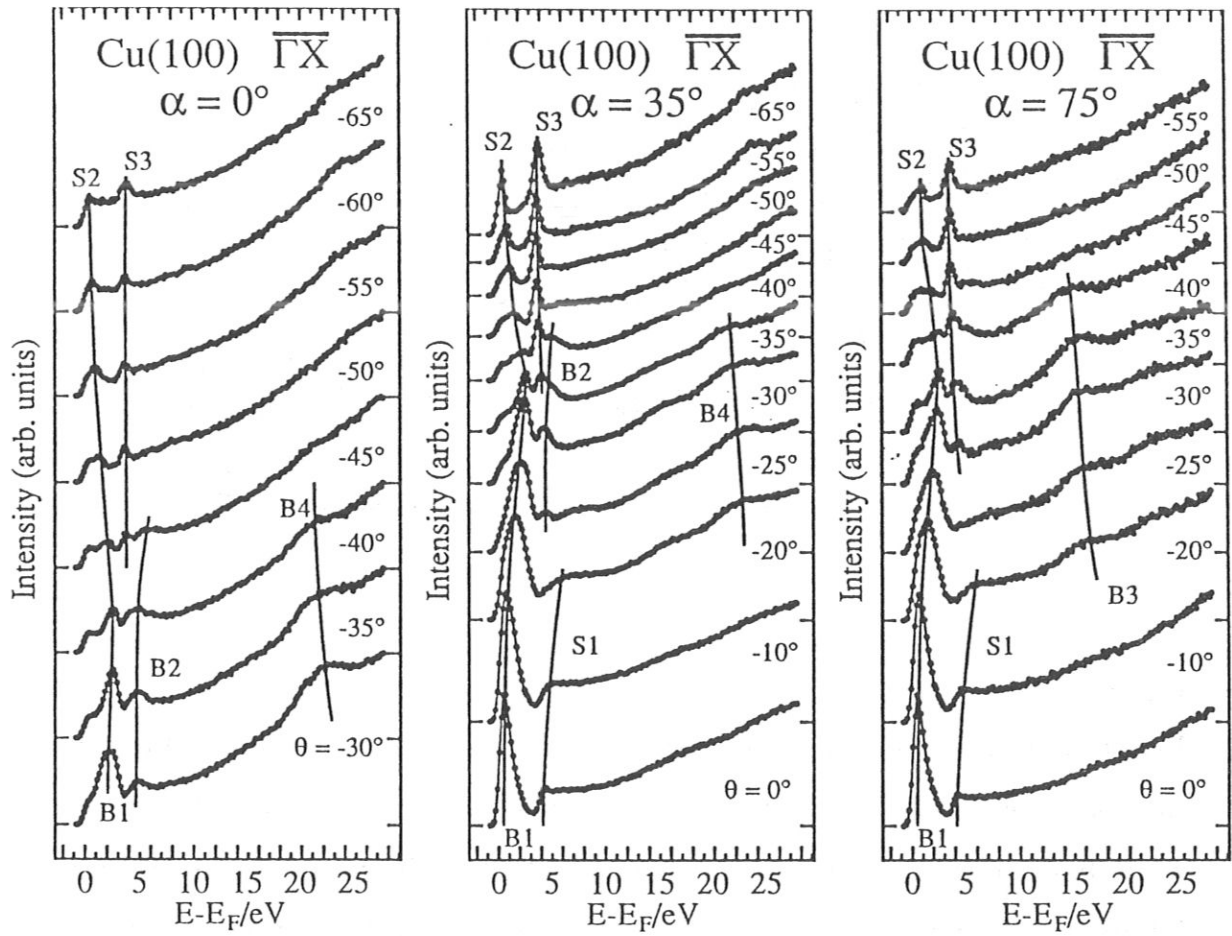


Figure (2.2):

IPE spectra from Cu(100) at various polar angles  $\theta$  of the electrons in the  $\overline{\Gamma X}$  direction for three photon take-off angles  $\alpha = 0^\circ, 35^\circ$  and  $75^\circ$ .

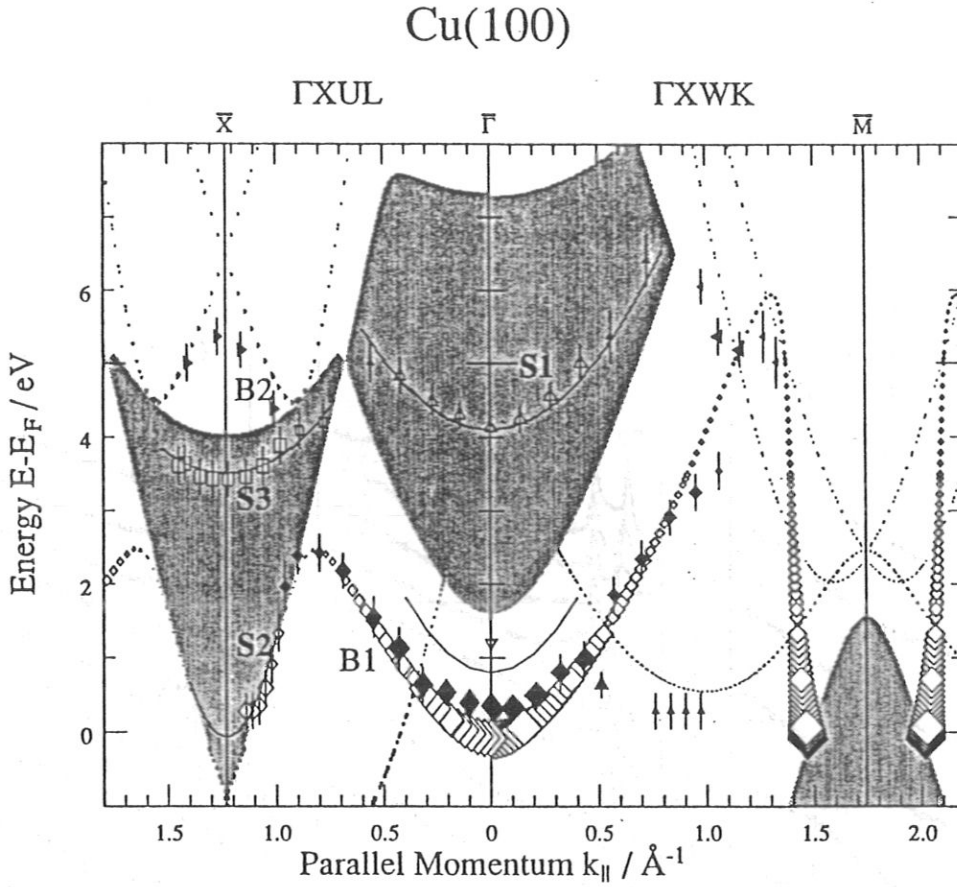


Figure (2.3):

$E(k_{\parallel})$  diagram for Cu(100). Transitions predicted from the combined interpolation scheme calculation are shown by the open symbols without error bars. The different symbols belong to transitions between different bands, characterized by the dominant plane wave component of the wavefunction of the initial and final state  $G_i$  and  $G_f$ . The experimental data for bulk transitions are shown as filled symbols with error bars. The size of the symbols indicates the intensity of the transition. The symbols of the measured bulk transitions were chosen to correspond to the calculated transitions. The band gaps of the projected bulk band structure are shown as grey shaded areas. The data for transitions into surface states are marked as open symbols with error bars.

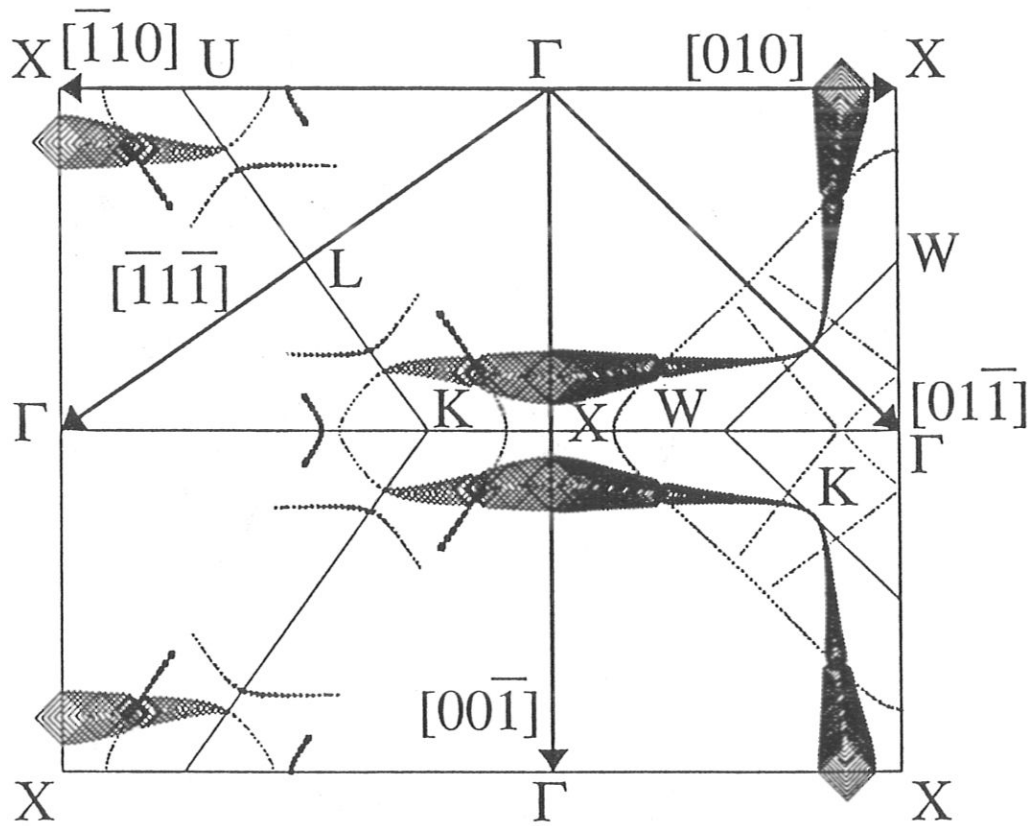


Figure (2.4):

Predicted k-space location of the transitions displayed in Fig. (2.3). The arrows indicate the directions of the surface normals. The size of the symbols is scaled with the square of the calculated matrix elements.

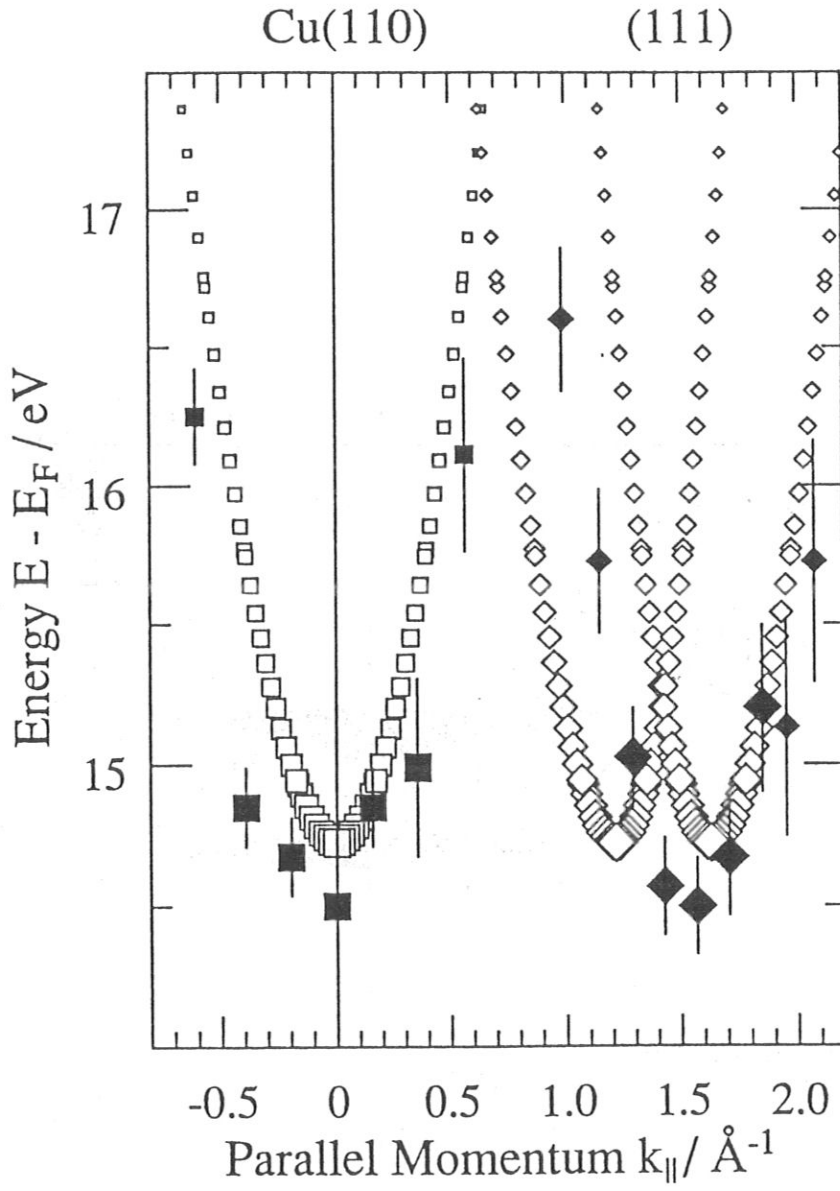


Figure (2.5):

$E(k_{\parallel})$  diagram for the higher energy bulk transition, which can be observed on Cu(110) (squares) and Cu(111) (diamonds). The open symbols are the results of the combined interpolation scheme calculation, the filled symbols with error bars show the experimental data.

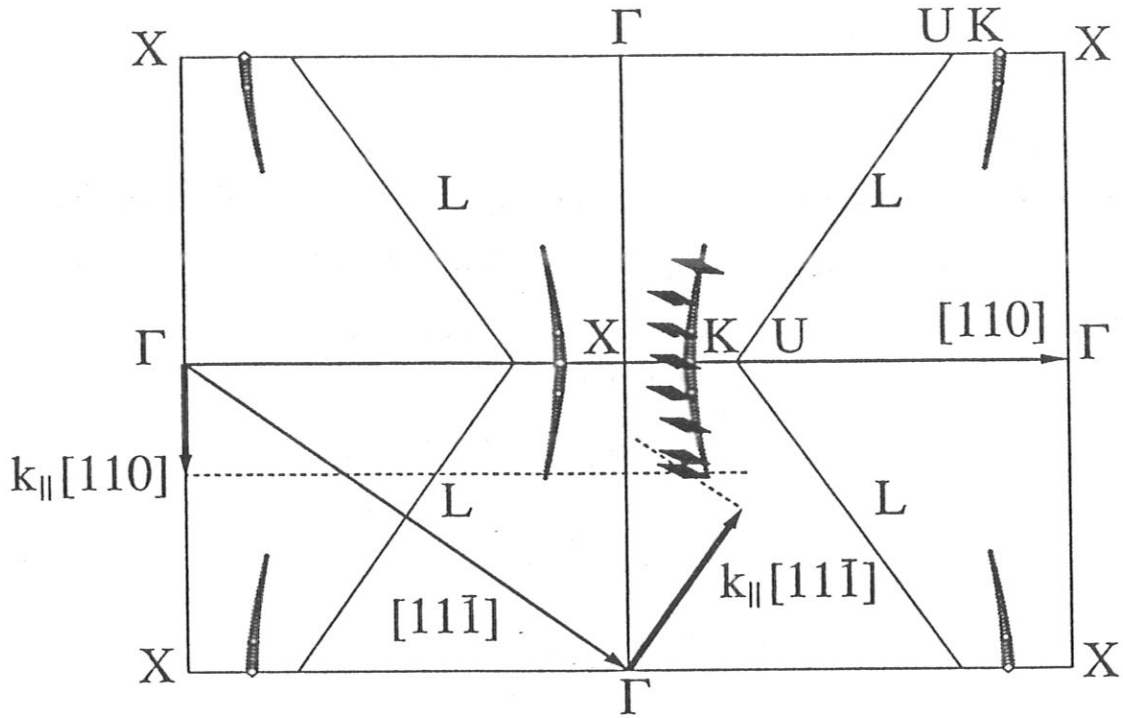


Figure (2.6):

Triangulation of the higher energy bulk transition of Fig. (2.5) in the  $\Gamma$ XUL mirror plane. The fat arrows indicate the  $k_{||}$ -directions for the (110) and (111) surface in the mirror plane, which are perpendicular to the surface normals marked as arrows. The results of the combined interpolation scheme calculation are shown as open diamonds.

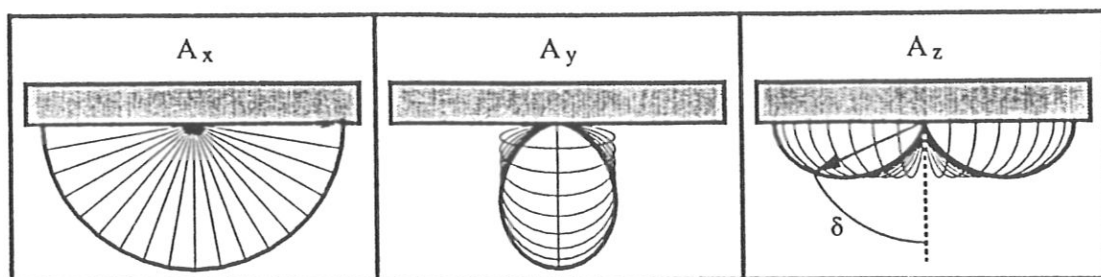


Figure (3.1):

Radiation angular distribution for pure  $A_x$ ,  $A_y$  and  $A_z$  dipole transitions.  $\delta$  is the angle between the dipole axis and the direction of the photon emission.

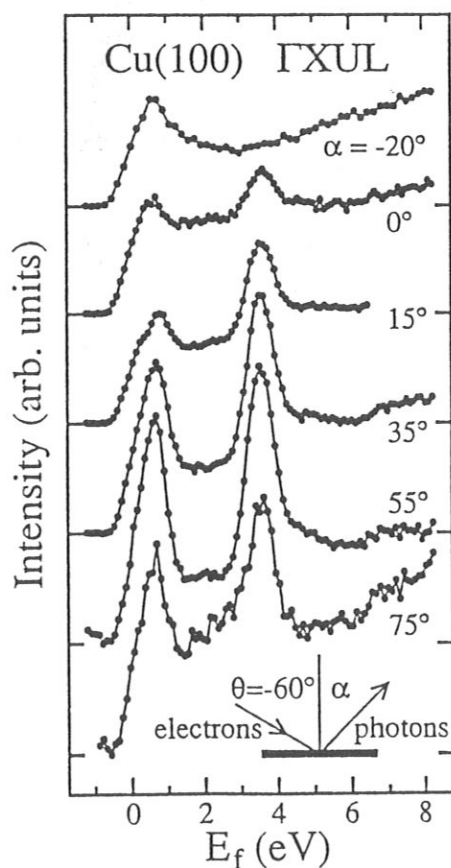


Figure (3.2):

Set of IPE spectra for various photon take-off angles  $\alpha$  normalized to equal intensity at a final state energy of  $E_f = 5.7$  eV. The electrons impinged at an angle  $\theta = -60^\circ$  relative to the surface normal of the Cu(100) crystal. Electrons and photons propagated in the  $\Gamma$ XUL mirror plane.

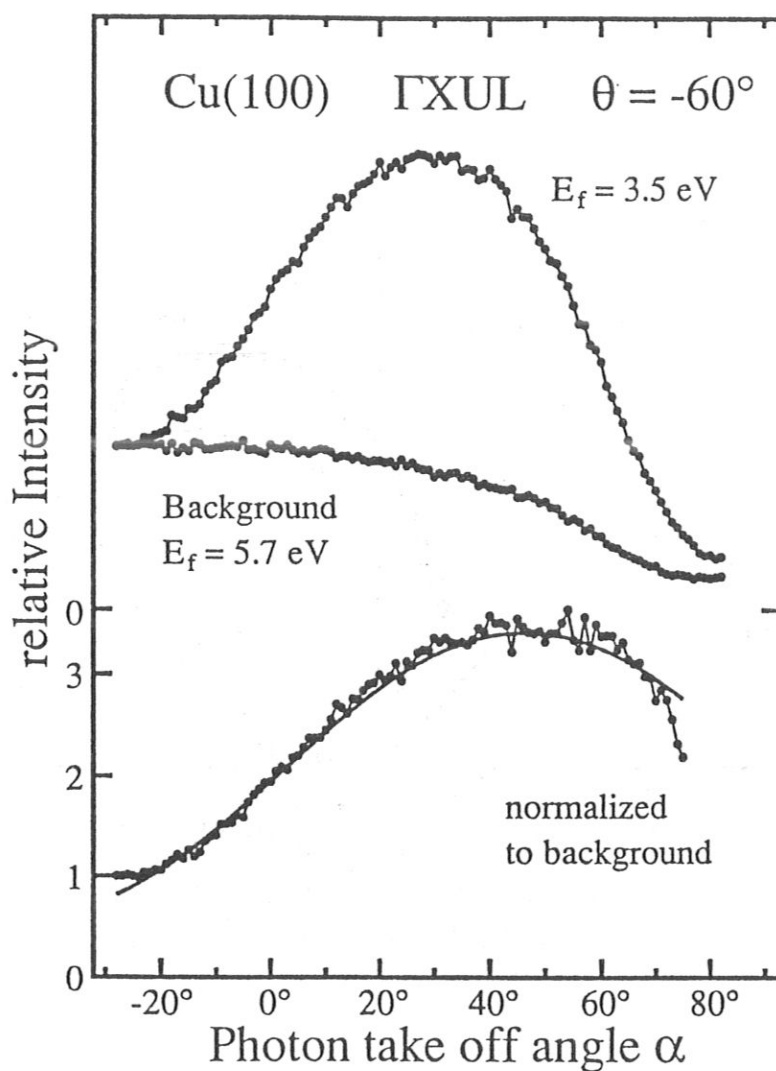


Figure (3.3)a:

Intensity of the surface state at  $E_f = 3.5$  eV and of the background at  $E_f = 5.7$  eV of Fig. (3.2) as a function of the photon take-off angle  $\alpha$  (upper part). In the lower part the intensity of the surface state normalized to the background as a function of the photon take-off angle  $\alpha$  is shown.



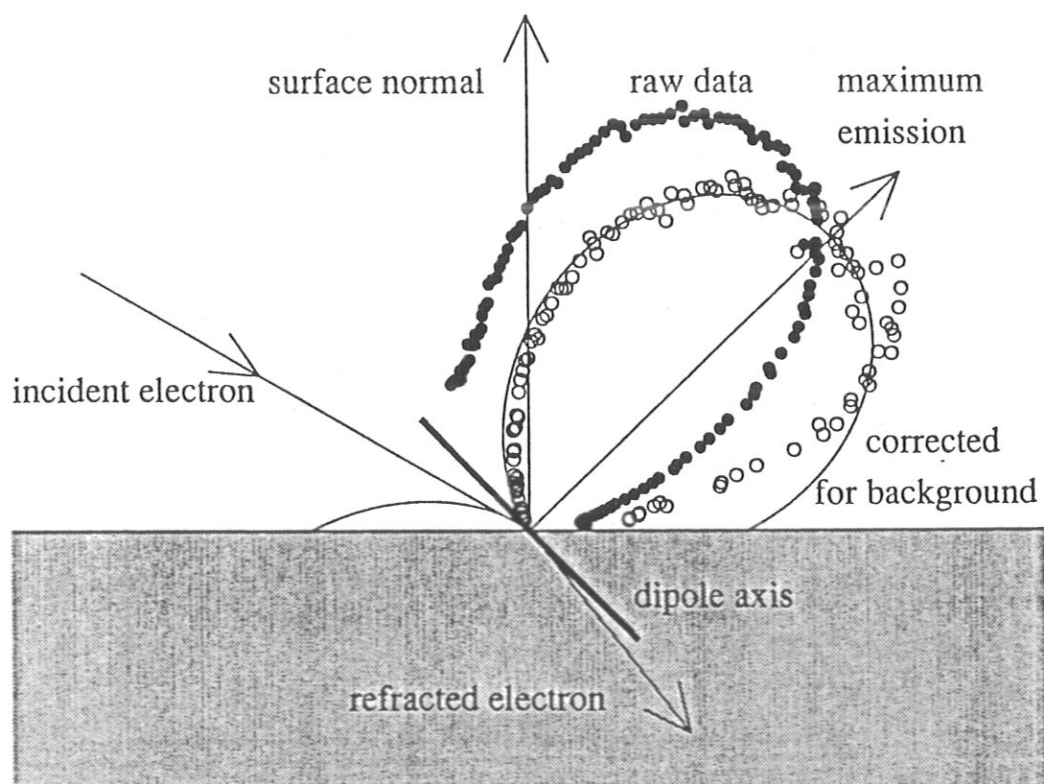


Figure (3.3)b:

Polar plot of the data for the surface state of Fig. (3.3)a.

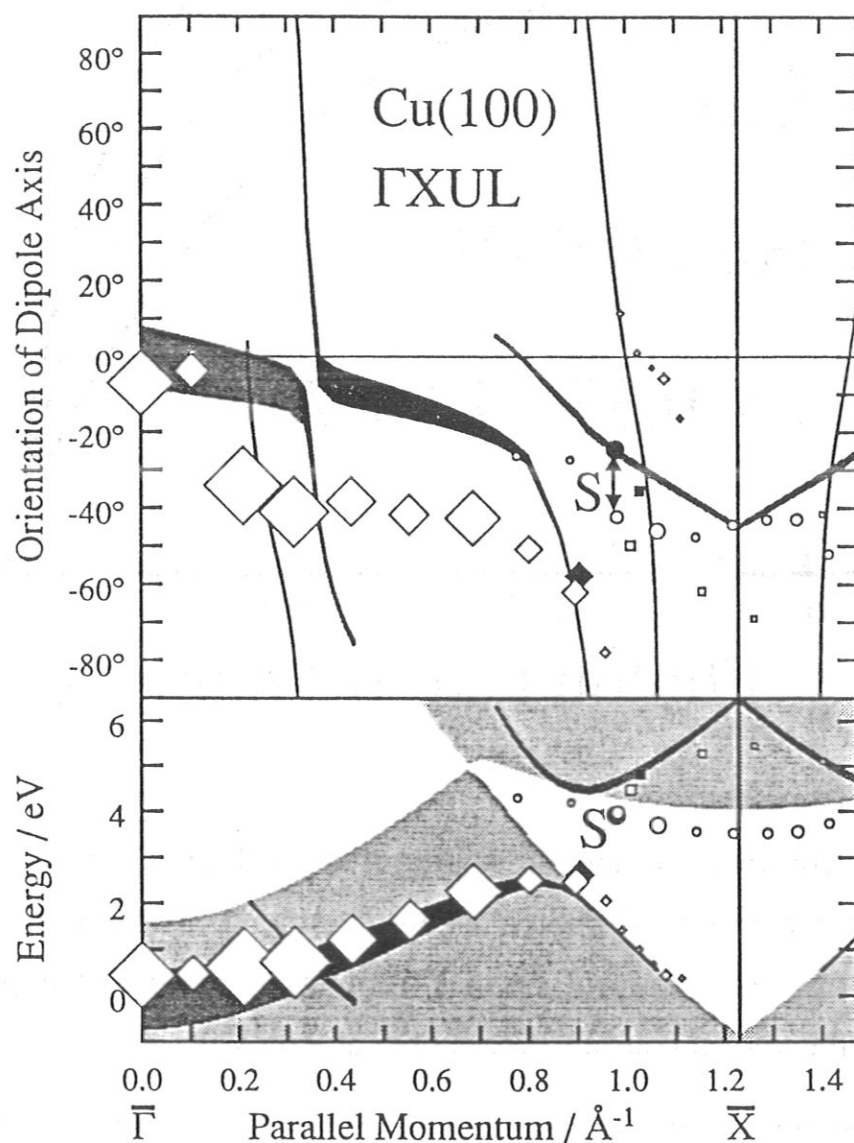


Figure (3.4):

Experimental data on Cu(100) in the  $\Gamma XUL$  mirror plane for the dispersion of transitions with 9.6 eV photon energy (lower part) and the orientation of the dipole axis of these transitions (upper part) are compared to the results of the combined interpolation scheme.

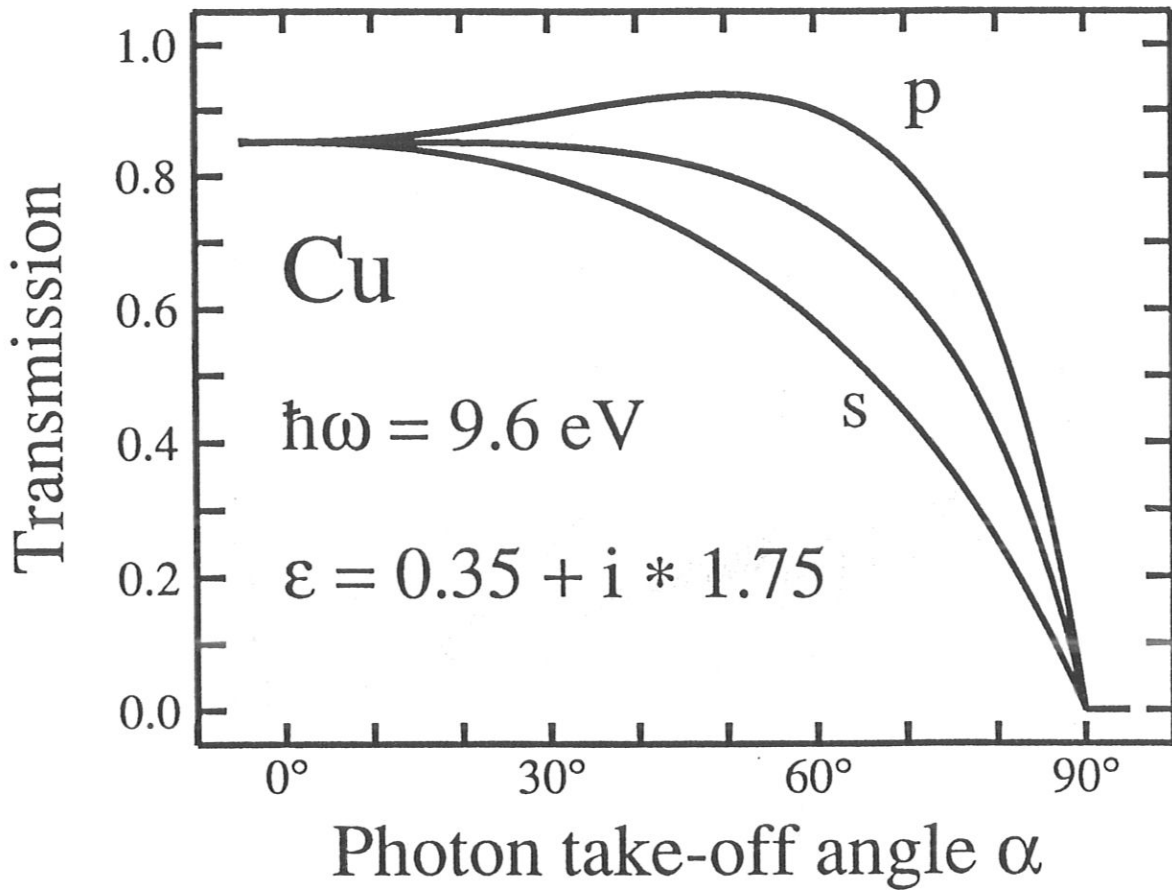


Figure (3.5):

Probability for transmission of a photon created in the solid into the vacuum as a function of photon take-off angle  $\alpha$ . The transmission is calculated from the classical Fresnel formulas for s, p and unpolarised light using the optical constants for copper at 9.6 eV.

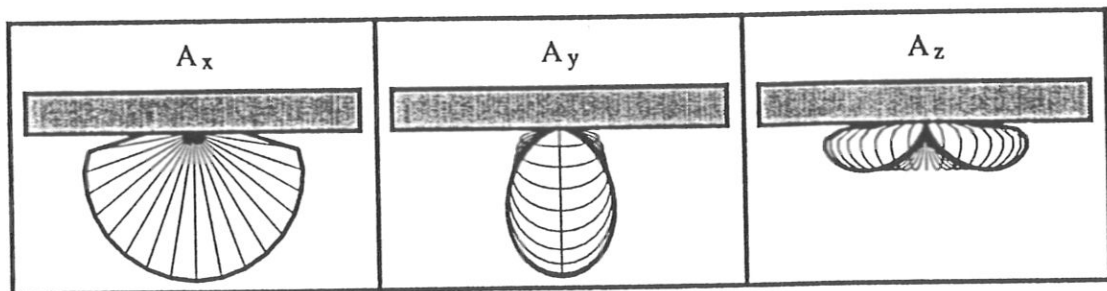


Figure (3.6):

Radiation angular distribution for pure  $A_x$ ,  $A_y$  and  $A_z$  dipole transitions corrected with the transmission for unpolarised background.

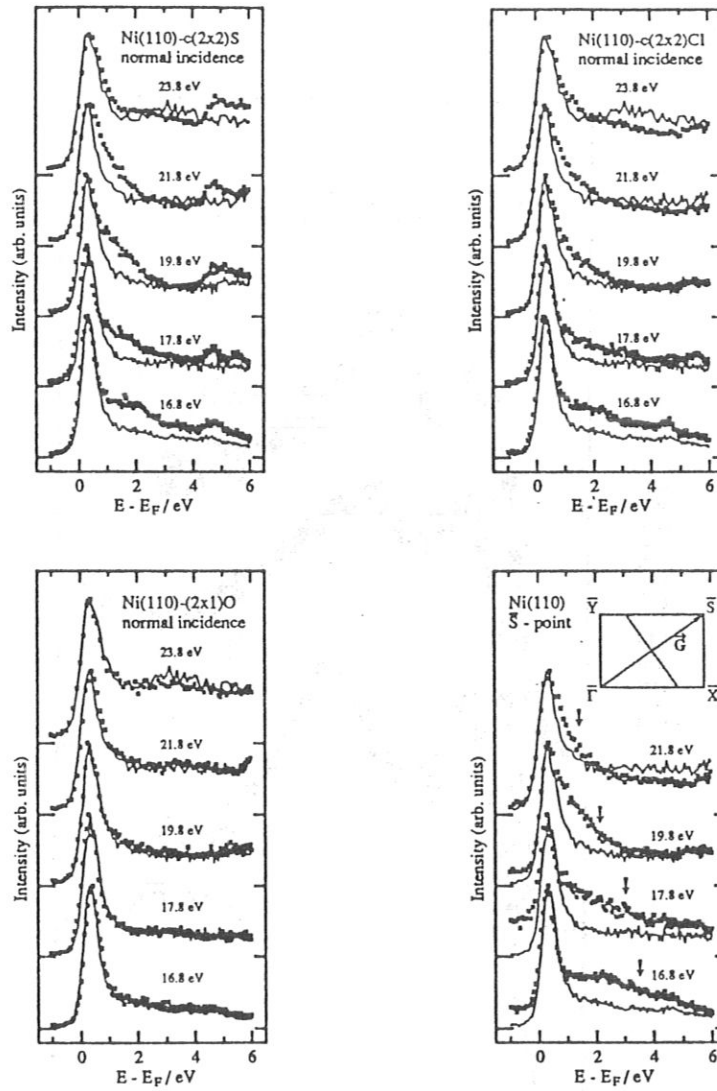


Figure (4.1):

Normal incidence IPE spectra at constant initial state energies for Ni(110). The upper left panel shows spectra for c(2x2)S overlayer, the upper right panel spectra for c(2x2)Cl overlayer and the lower left panel spectra for (2x1)O overlayer. The spectra of the clean surface are shown as full lines. The spectra of the clean surface at the  $\bar{S}$  point can be seen in the lower right panel.

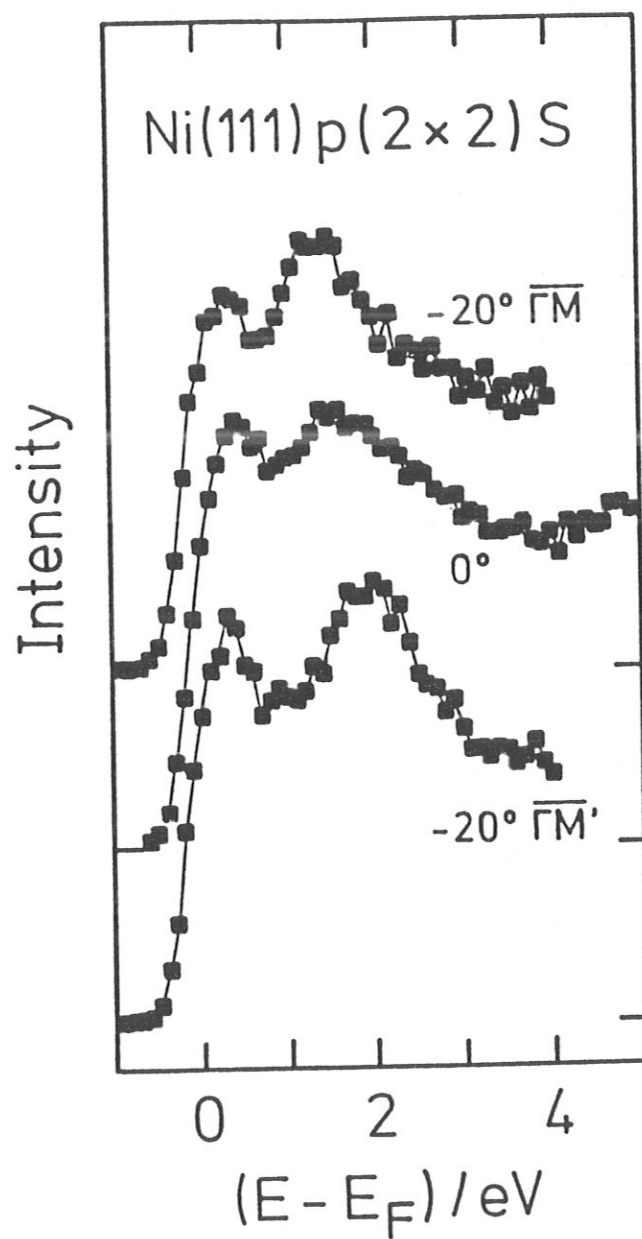


Figure (4.2):

IPE spectra from a  $p(2 \times 2)$  sulphur covered  $\text{Ni}(111)$  surface.

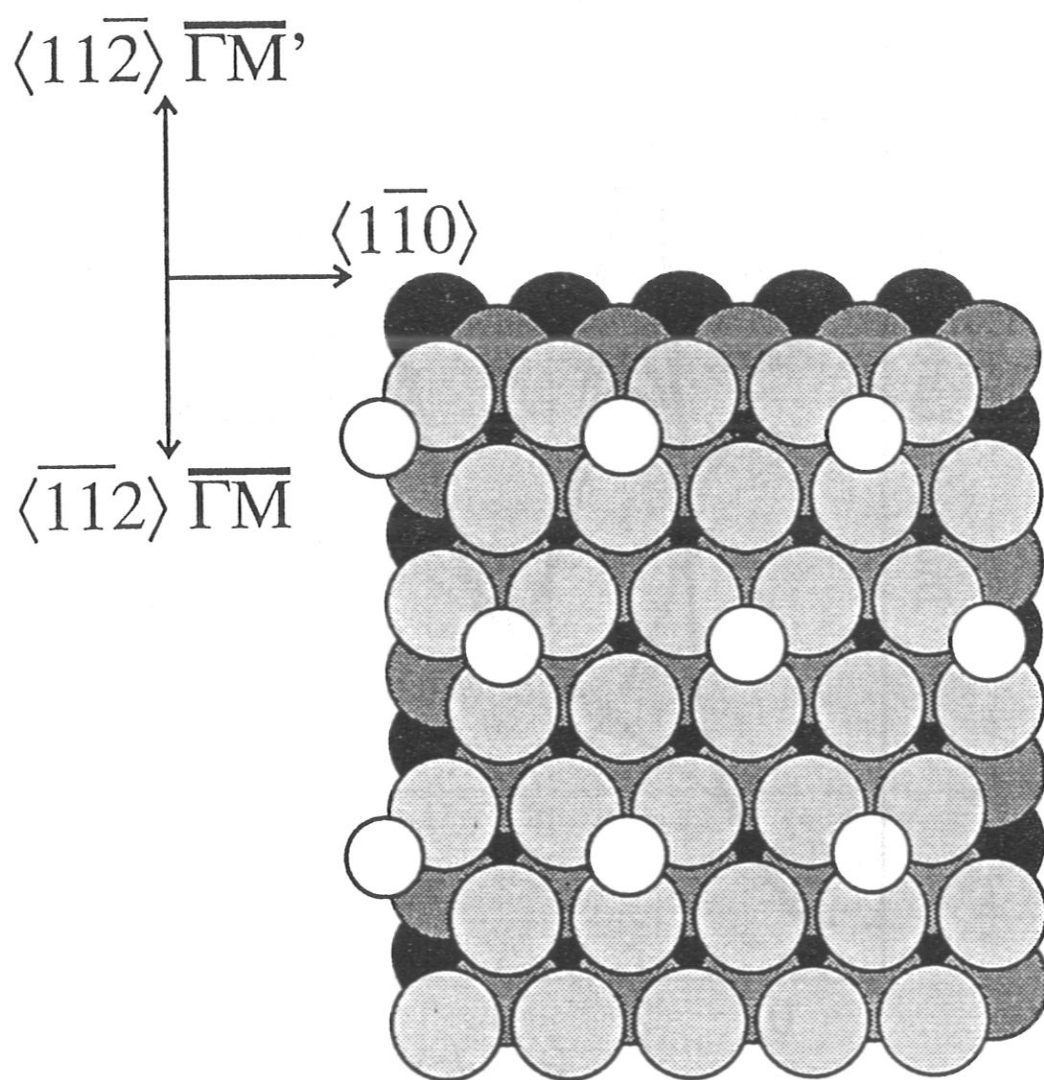


Figure (4.3):

Face centered cubic (111) surface with a p(2x2) adsorbate structure.

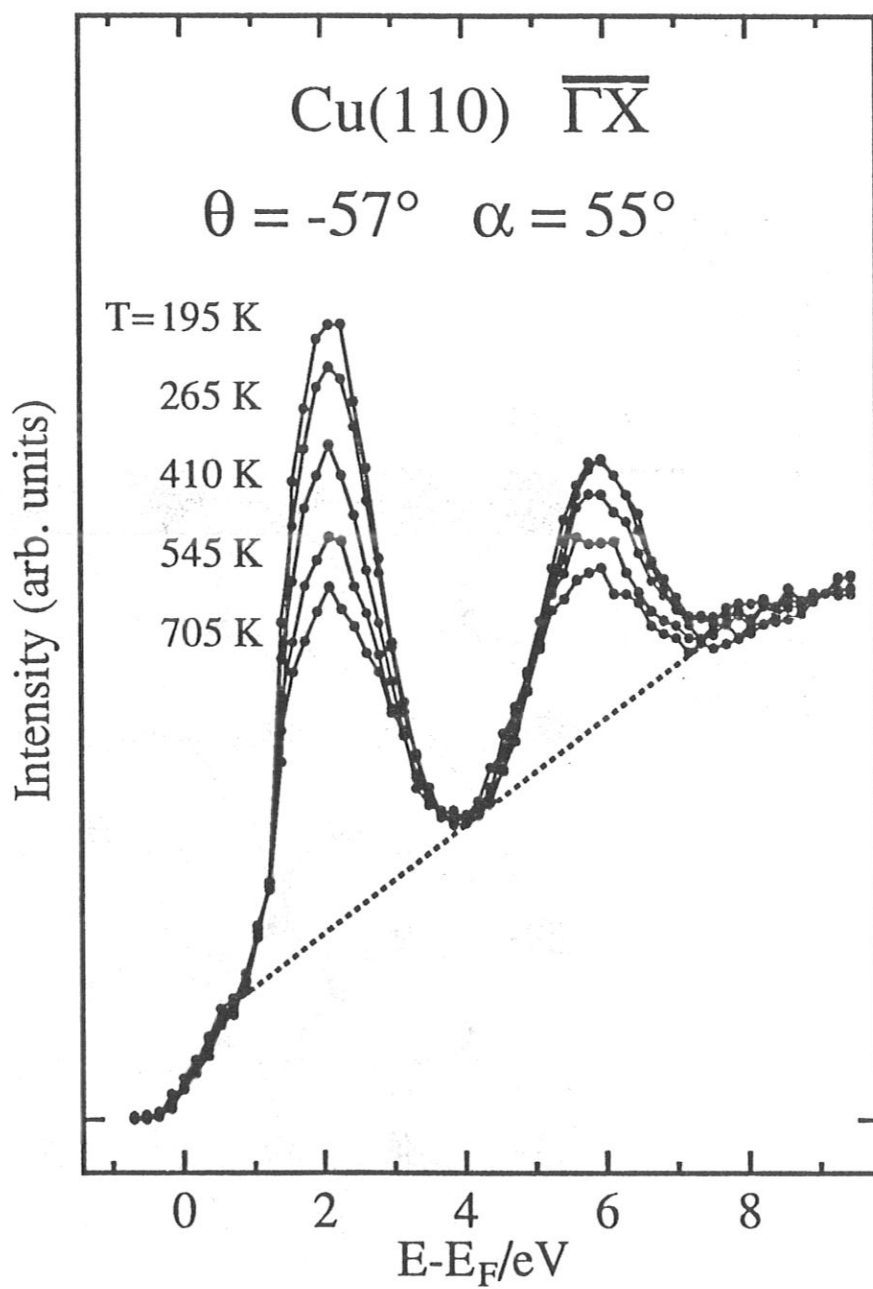


Figure (5.1):

Set of IPE spectra for Cu(110) for several temperatures. The estimated background is indicated by the dashed line.



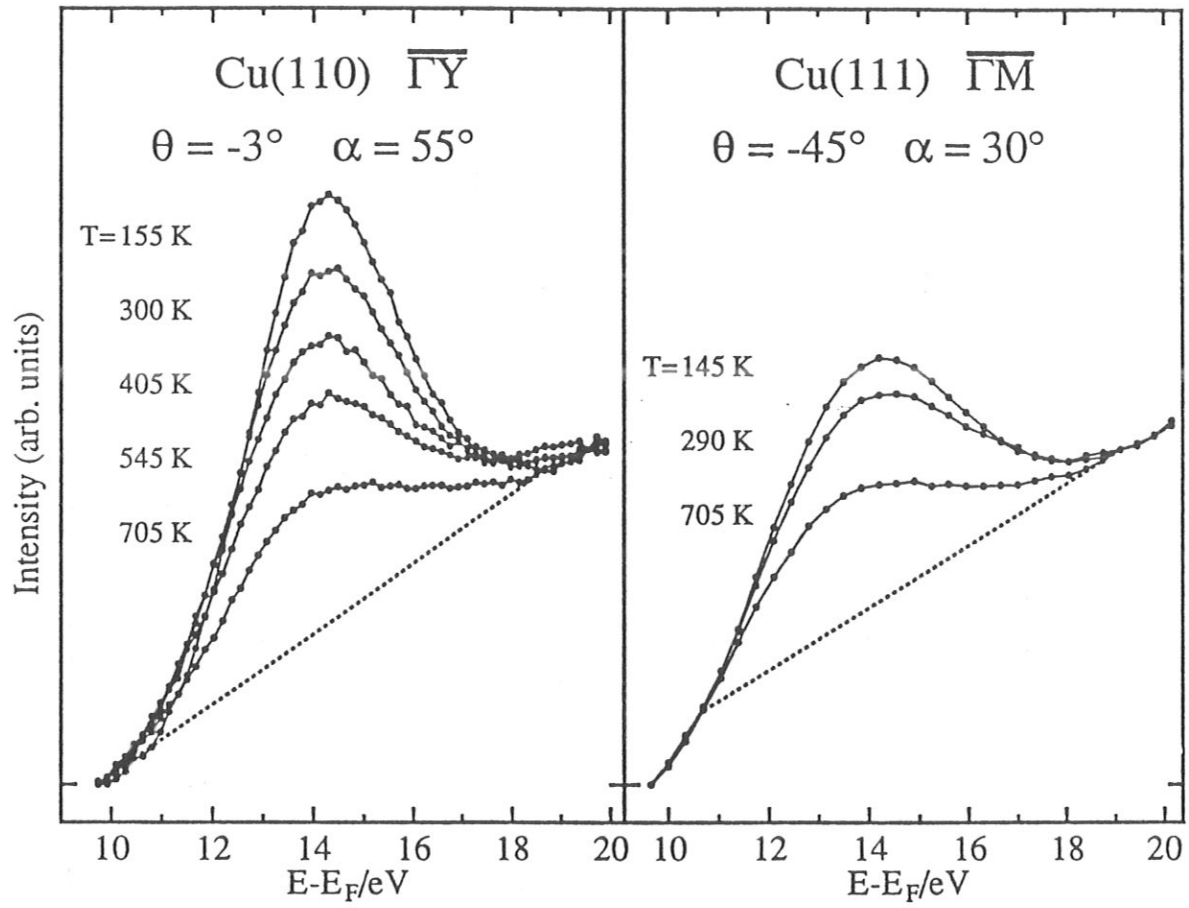


Figure (5.2):

Inverse photoemission spectra for a selected bulk transition observed on two different surfaces for various sample temperatures.

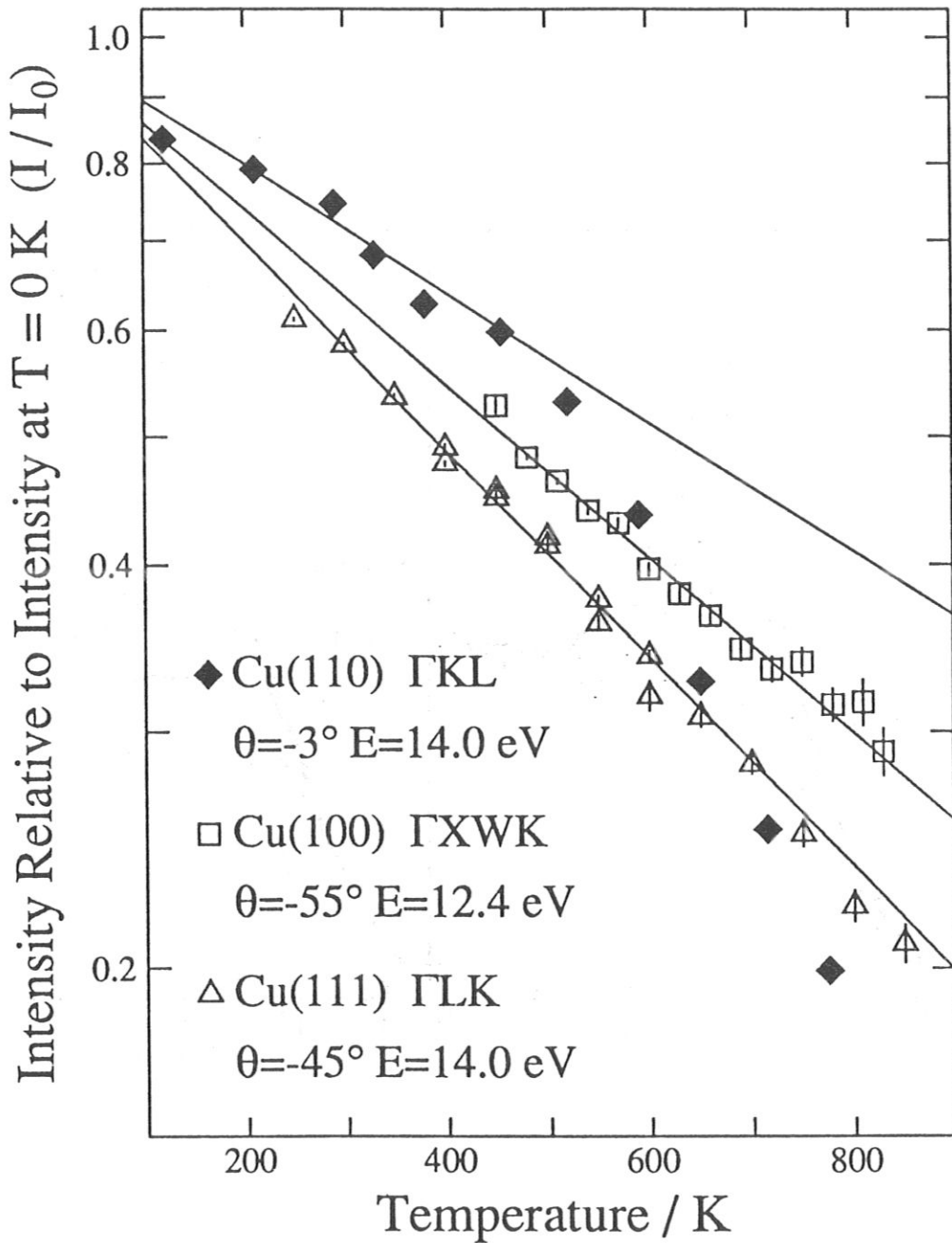


Figure (5.3):

Semilogarithmic plot of the temperature dependence of the intensity of the transitions of Fig. (5.2) and of a bulk transition on Cu(100). The straight lines are linear fits for the temperature range from 200 K to 900 K for Cu(111) and Cu(100). The fitting range is restricted to temperatures less than 400 K for Cu(110).

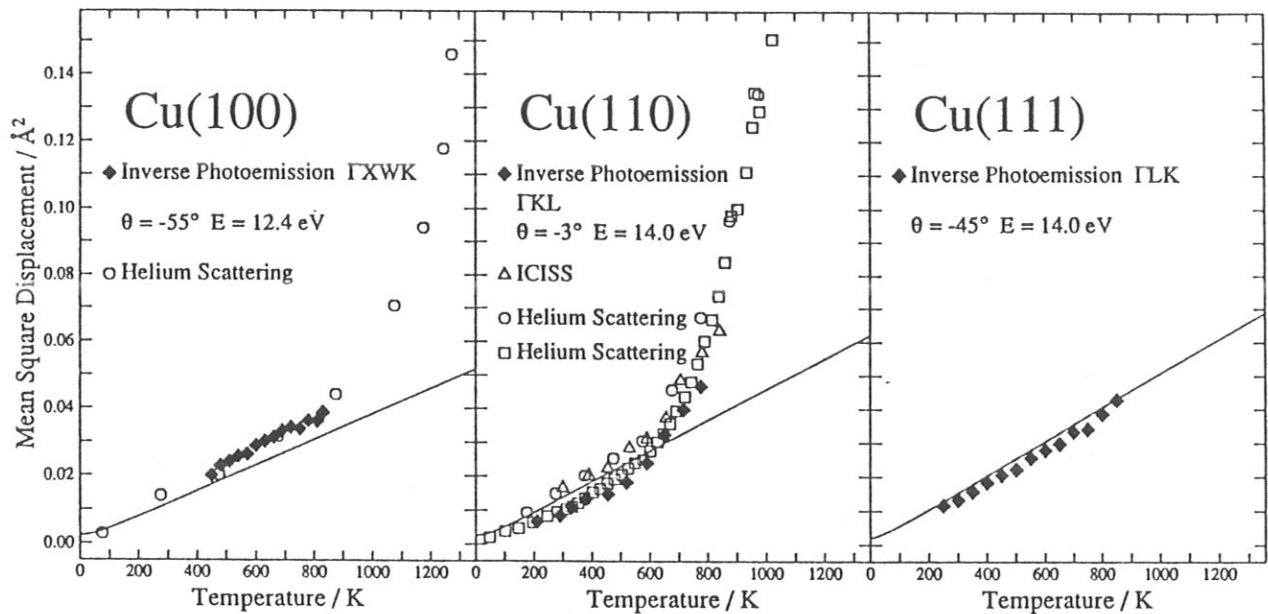


Figure (5.4):

Mean square displacements of surface atoms as a function of temperature for the three low-index copper surfaces. The IPE data agree well with results from He atom [5.8-9] and ion scattering [5.10] measurements. Phonon calculations agree with the measured data only at low temperatures.

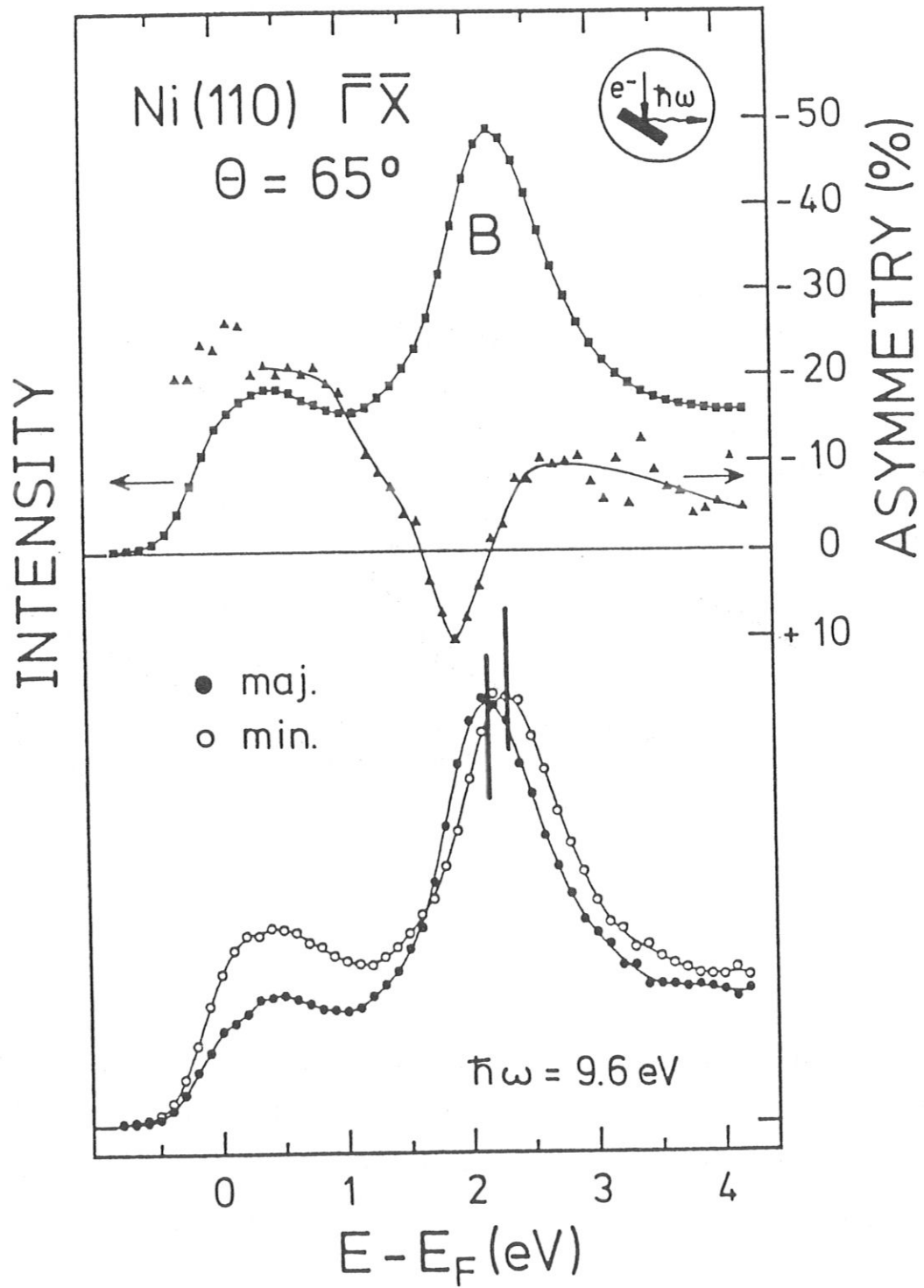


Figure (6.1):

Spin splitting of a bulk transition for an sp-like final band.

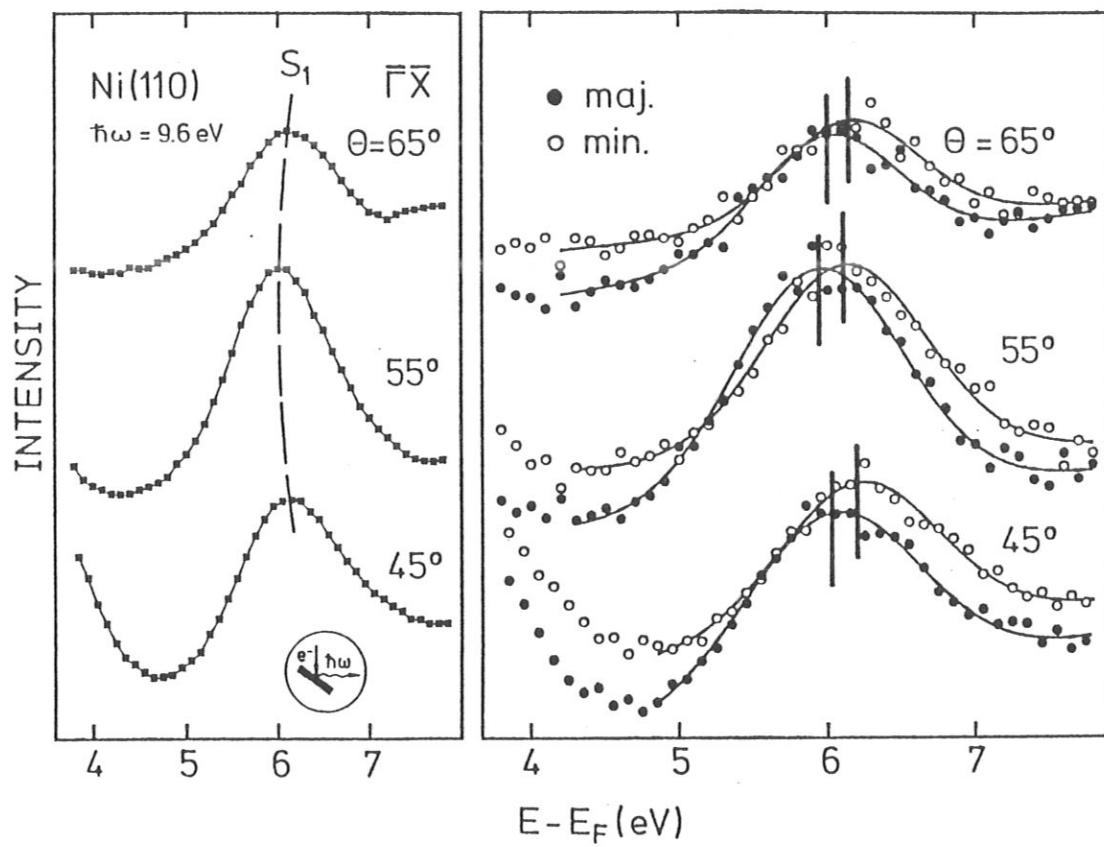


Figure (6.2):  
Spin splitting of a crystal-induced surface state.